Chapter 2

Recirculation and retention on the shelf in St. Helena Bay

In this chapter, we will concentrate on the first question listed in the summary of the first chapter: "Why is St. Helena Bay such a successful nursery ground ?". The shelf being large in St. Helena Bay, idealised barotropic numerical experiments are conducted in order to explore the interactions between an equatorward, upwelling favorable, wind forced current and the topogaphy of the Bay. Diagnostic analysis and analytical calculations bring to light the dynamics involved in the simulations. The impact of the circulation on the retention of biological material in the Bay is explored through a tracer marking the age of the water masses.

Dans ce chapitre, nous nous concentrerons sur la première question énoncée dans le résumé du chapitre pr'ecédent: "Quelle est la cause du succès de la nourricerie de la Baie de Ste Hélène ?". La Baie de Ste Hélène présentant un large plateau, des expériences idéalisées barotropes sont mises en place afin d'explorer les interactions entre un courant vers l'équateur, forcé par un vent favorable a l'upwelling, et la topographie de la baie. Des analyses diagnostiques, et des calculs analytiques éclairent la dynamique impliquée durant les simulations. L'impact de la circulation sur la rétention des composantes biologiques est quantifiée à l'aide d'un traceur représentant l'age des masses d'eau.

The upwelling of the West Coast of South Africa provides the necessary enrichment for the recruitment. But the driving mechanism of coastal upwelling, the offshore Ekman transport, at the same time, advects the larvae away from the productive area. Hence, the success of recruitment requires the presence of a retention process that keeps the larvae in the favorable area [*Bakun,* 1998]. If enrichment by upwelling occurs all along the West Coast, the success of St. Helena Bay should be related to presence of retention in the bay.

St. Helena Bay is located just North of Cape Columbine, one the two major capes of the West Coast. It can be seen as a step-like indentation of 100 km in the coastline. Associated with this topographic feature, the shelf broadens dramatically, to reach a width of 150 km (figure 1.3). This topographic configuration should alter the coastal circulation in a favorable way for the recruitment.

To test this last statement, 2 hypotheses are assumed. Firstly, on a broad relatively flat shelf like St. Helena Bay, following the criterion of Clark and Brink [1985], baroclinic processes should be of less importance than barotropic dynamics. Secondly, spatial and temporal wind variations, although important, should not be necessary to produce a favorable environment during upwelling events.

Following these hypotheses, a set of idealized numerical experiments are undertaken to explore the influence of a cape and a broadening shelf on the retention during the upwelling season (e. g. for a coastal circulation forced by an equatorward wind).

The outline of this chapter is as follow. After a review of the interaction between coastal currents and capes, a description of the numerical model is provided. An analytical model of the barotropic processes gives characteristic values for velocities and free surface elevation. Outputs of a reference numerical experiment are analyzed and sensitivity tests are conducted, using a range of values for wind forcing, bottom friction or different size of capes. Different mechanisms, such as control by bottom friction or the generation of standing waves, are tested to explain the flow patterns observed in the experiments. Finally, a tracer showing the age of the water is integrated into the model to quantify retention.

2.1 Interactions between coastal currents and capes

Interactions between capes and coastal currents are complex and remain poorly understood; although they have been studied in many ways. Crepon et al. [1984] solved analytically a linear upwelling two-layer model around a rectangular promontory. Baroclinic and barotropic Kelvin waves generated at the corner of the cape propagate poleward and can lead to upwelling fluctuations independent of local winds. Further, they relate the poleward undercurrent to the difference of the phase speeds between baroclinic and barotropic waves. They found numerically the same pattern with different shapes of cape. Batteen [1997] explains the enhancement of upwelling equatorward of capes by conservation of potential vorticity in equatorward flows. Downstream and inshore of the plume of upwelled water, an "upwelling shadow" can be found such as that described by Graham and Largier [1997] for Northern Monterey Bay where warm water is trapped at the coast behind a narrow oceanic front.

Several laboratory experiments involved flow past capes. Davies et al. [1990] introduced stratification in the case of a flat bottom and no rotation. Whereas stratification determines all aspects of eddy generation or eddy shedding from the capes, bottom friction seems to be crucial during the decay of the eddy [*Davies et al.,* 1990]. By introducing a counterclockwise rotation, Boyer and Tao [1987a] showed that the response of the flow differs dramatically if the cape is on the left or on the right looking downstream in the Northern hemisphere. Their setting corresponds to respectively an equatorward and poleward flow along an oceanic

Eastern boundary. The poleward current passes through three regimes, depending on the Burger number ($S = \frac{N^2H^2}{f^2L^2}$; where N^2 is the Brunt-Väisälä frequency, H is the water depth, f is the Coriolis parameter and L a characteristic length scale):

Small S: flow fully attached, no eddy generated;

Medium S: generation of an attached anticyclonic eddy;

Larger S: shedding of anticyclonic eddies.

For the equatorward current, there is no fully attached regime:

Small S: generation of an attached cyclonic eddy (quickly formed but subsequently spins down);

Larger S: shedding of cyclonic eddies.

Boyer et al. [1987b] have performed the same kind of experiments with an obstacle on the left or on right of the flow, but involving this time an homogeneous fluid. They found a complex wake motion for a certain range of Rossby and Ekman parameters, and again strong differences if the cape is on the left or on the right. In the case "cape on the left", the vortex shedding is more regular, but in both cases, eddies can merge into larger structures that can be, depending of the parameters, attached, shed or advected downstream. Klinger [1983] has tested the influence of the Rossby and Ekman numbers on the formation of anticyclones on slopes, by concentrating on a barotropic flow past a corner in a rotating tank (poleward flow along an eastern boundary). In this case, whereas the gyre size is approximately proportional to the Rossby number, it is not strongly influenced by bottom friction.

Narimousa and Maxworthy [1989] have built a more realistic laboratory model to interpret satellite observations of coastal upwelling. This experiment shows the effects of ridges and capes on the generation of standing waves, meanders, filaments and eddies. The capes produce cyclones inshore and filaments offshore. These experimental results are in good agreement with satellite images of sea surface temperature off the West Coast of the North American continent. To describe the patterns measured in the lee of islands, Wolanski et al. [1984] have introduced an "Island wake parameter": P from an Ekman pumping model for the control of wake eddies. This parameter can predict if friction dominates the flow (P<1), if there is a stable wake (P$\sim$1) or if there is apparition of instabilities (P>1). This result has been found to be in good agreement with the flow patterns derived from remotely sensed imagery by Pattiaratchi et al. [1986], but has been in bad agreement when bottom topography is complex.

Similar studies have been conducted using numerical models. Becker [1991] built a numerical model of a viscous flow past a cylinder in a rotating frame, when the Rossby (Ro) and the Ekman (Ek) numbers are small. She has found two key parameters for the boundary layer separation: $\lambda = \frac{Ro}{2\sqrt{Ek}}$, which is an equivalent of the "Island wake parameter" and δ the boundary layer thickness. The flow starts to detach when $\lambda > 1$, and the bubble length increases linearly with λ and with decreasing δ. The generation and evolution of eddies around headlands by a tidal flow have been studied analytically and numerically by Signell and Geyer [1991]. In a boundary layer model, detachment occurs because of bottom friction as soon as an adverse pressure gradient is established. They found using a 2D numerical model that the extent of vorticity is limited by the frictional length scale: $l_f = \frac{H}{2C_D}$. In a two layer realistic numerical model of Oregon coast, Peffley and O'Brien [1975] showed that bottom topography

overwhelms coastline irregularities in the generation of mesoscale upwelling features. On the contrary, using a realistic 3D numerical model of the California upwelling system, Batteen [1997] found that wind forcing and coastline irregularities are key mechanisms for the generation of meanders, eddies, jets and filaments. She showed that capes "anchor" filaments and generate cyclonic eddies. The process of generation and control of a cyclonic eddy past Point Conception (California) has been studied by Oey [1996]. In a one and a half layer, reduced-gravity model (infinite bottom layer), equatorward wind forced currents generate a cyclonic eddy past the cape by advection of vorticity at the corner. Viscosity and the Rossby number control it. This eddy is found again in a 3D realistic model of the Santa Barbara Channel. It seems to follow the same processes of formation, although bottom topography and beta effect are shown to become important for longer time period (> 30 days).

A main discrepancy between our study and Oey's [1996] work is the width of the shelf in St Helena Bay that extends from 50 km to 150 km, while the extension of the shelf in front of Point Conception is limited to 20 km. The presence of those shallow waters invalidate the use of a one layer and a half reduced gravity model, and bottom effects should be important in the generation and control of cyclonic eddies. It appears then that the presence and the shape of the bottom topography should overwhelm the effects related to stratification. To quantify this, the Brunt-Väisälä frequency N^2 has been calculated using recent temperature and salinity measurements in St. Helena Bay. It has a typical value of $7 \times 10^{-3} s^{-1}$. Whereas stratification is significant, the gentle bottom slope of St. Helena Bay (slope coefficient: $\alpha \sim 0.2$ %) satisfies the dynamic criterion for barotropic shelf water response [*Clark and Brink,* 1985]: $\frac{N^2\alpha^2}{f^2} \ll 1$, where f is the Coriolis parameter. In St Helena Bay, $\frac{N^2\alpha^2}{f^2} \sim 0.05$. This 'bottom slope' Burger number allows us to state that whereas density related processes such as upwelling and associated baroclinic coastal jets might be important, the major characteristics of the circulation can be described by barotropic dynamics. This is consistent with the barotropic nature of the flow measured by Lamberth and Nelson [1987].

In this chapter, we will only concentrate on the barotropic response of a coastal ocean to equatorward wind forcing. Baroclinic effects are expected to be secondary or localized [*Graham and Largier,* 1997] and will be investigated in future work. The aim of this chapter is to understand the processes controlling the pattern of flow detachment and eddy generation in the vicinity of Cape Columbine.

2.2 Model description

The numerical code is the barotropic part of the SCRUM 3D oceanic model from Rutgers University [*Song and Haidvogel,* 1994, *Hedström,* 1997]. The model is based on the hydrostatic and Boussinesq approximations. The barotropic component solves the vertically integrated momentum equation [*Hedström,* 1997] and in our case density variations are not taken into account. SCRUM conserves the first moments of u and v. This is accomplished by using the flux form of the momentum equations [*Hedström,* 1997]:

$$\frac{\partial}{\partial t}(D\bar{u}) + \frac{\partial}{\partial x}(D\bar{u}\bar{u}) + \frac{\partial}{\partial y}(D\bar{u}\bar{v}) - Df\bar{v} = -gD\frac{\partial \zeta}{\partial x} + \nu_4 \hat{\triangle}\left(\frac{\hat{\triangle}(\bar{u})}{D}\right) + \frac{\tau_x}{\rho} - r\bar{u} \qquad (2.1)$$

$$\frac{\partial}{\partial t}(D\bar{v}) + \frac{\partial}{\partial x}(D\bar{u}\bar{v}) + \frac{\partial}{\partial y}(D\bar{v}\bar{v}) + Df\bar{u} = -gD\frac{\partial \zeta}{\partial y} + \nu_4 \hat{\triangle}\left(\frac{\hat{\triangle}(\bar{v})}{D}\right) + \frac{\tau_y}{\rho} - r\bar{v} \qquad (2.2)$$

Where $\hat{\triangle}$ is the operator:

$$\hat{\triangle}(A) = \frac{\partial}{\partial x} D \frac{\partial A}{\partial x} + \frac{\partial}{\partial y} D \frac{\partial A}{\partial y} \tag{2.3}$$

The continuity equation takes the from:

$$\frac{\partial \zeta}{\partial t} + \frac{\partial}{\partial x}(D\bar{u}) + \frac{\partial}{\partial y}(D\bar{v}) = 0 \tag{2.4}$$

Where:

x is the along shore coordinate (positive towards the equator).

y is the cross-shore coordinate (positive towards the open ocean).

$\bar{u}$ and $\bar{v}$ are the vertically averaged flow velocity respectively in each coordinate direction.

ζ is the free surface elevation.

D is the total water column depth, $D = H + \zeta$, where H is the ocean depth.

f is the Coriolis parameter, $f = 2\Omega sin\phi$, where Ω is the Earth angular velocity and ϕ is the latitude. In our case, because the time scale O(10 days) and the length scales O(100 km) are small enough, we can assume a constant Coriolis parameter as explained by Kundu [1990]. $f = -7.707 \times 10^{-5}$ s^{-1} at Cape Columbine.

g is the Earth gravity acceleration, $g = 9.81$ m.s^{-2}.

ν_4 is the lateral biharmonic constant mixing coefficient (m^4.s^{-1}).

r is the linear bottom drag coefficient (m.s^{-1}).

$\frac{\tau_x}{\rho}$ and $\frac{\tau_y}{\rho}$ are the kinematic surface momentum fluxes (wind stress) respectively in each coordinate direction (m^2.s^{-2}).

In order to preserve the mesoscale structures, a bi-harmonic operator parameterizes the horizontal viscosity. For the sake of simplicity and as suggested by Csanady [1982], the weak tidal currents are not resolved and the bottom stress is chosen to be proportional to the barotropic velocities. The linear bottom friction coefficient is initially fixed at a typical value found in the literature ($r = 3 \times 10^{-4}$ m.s^{-1}), but sensitivity tests have been conducted to explore the strong impact of this coefficient on the circulation.

The regular grid has a 5 km resolution along shore and cross-shore. The coastline is represented by a free-slip wall in x=0 and its variations are modelized by masking the inshore grid points where the depth is less than 50 m [*Hedström,* 1997]. The most straightforward way to close the domain offshore and on the sides is the use of a periodical channel: a free-slip wall far beyond the shelf break and all the outflows (inflows) at the southern boundary being inflows (outflows) for the northern boundary. Those boundary conditions allow an along shore wind forced circulation and conserve mass. The presence of the shelf break should isolate the shelf circulation from the effects of the offshore wall [*Csanady,* 1978]. The bottom topography is represented by a set of analytical functions which retains the main topographical features, thus focusing attention on the effects of Cape Columbine and the widening shelf on the circulation. The bathymetry has been made periodic to allow the use of the periodic channel (figure 2.1). Nevertheless, this topography is still comparable for the first 300 km to the

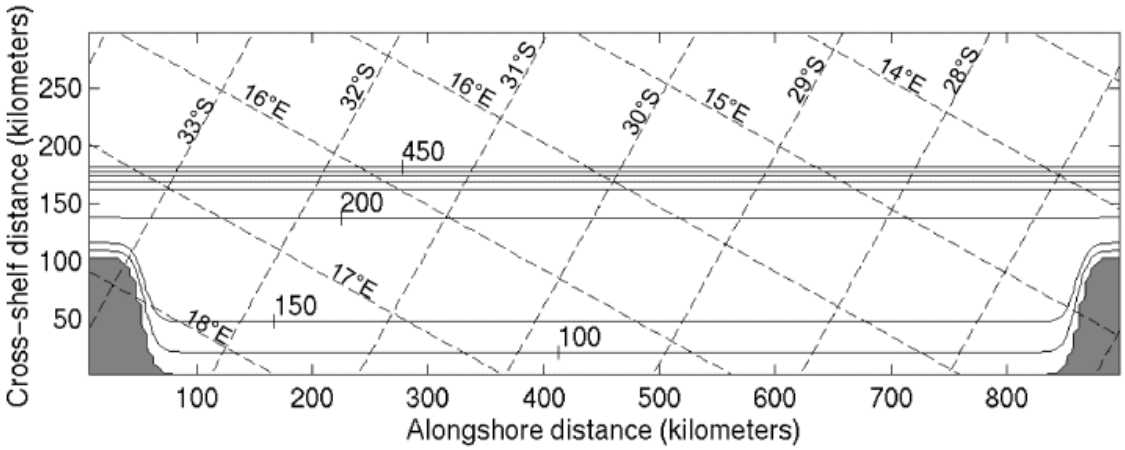

Figure 2.1 The periodic analytical bathymetry implemented in the model.

topography of St Helena Bay (see figure 1.3). The second cape on the right might perturb the solution at distances up to 300 km (the external Rossby radius) upwind of the cape, thus interfering with our area of interest. For this reason, the experiments are run with an along shore domain of 900 km. The atmospheric forcing is a constant wind stress parallel to the x-axis, accounting for the summer southeaster wind. The wind stress is uniform in space and constant in time for a given experiment. A set of runs with wind stress ranging from 0.02 $N.m^{-2}$ to 0.2 $N.m^{-2}$ are performed to investigate the effects of the intensity of the wind forcing.

2.3 Analytical expectations

To illustrate the basic mechanism for wind forcing in the coastal ocean, Brink [1998] solved a linearized along shore wind forced model where the spatial scales are small enough compared to the external Rossby radius of deformation to neglect divergence, and where the along shore scales are large compared to the cross-shore ones (boundary layer approximation, [*Csanady,* 1998]). This implies that the along shore flows are much stronger than the cross-shelf ones [*Brink,* 1998]. This is not true near Cape Columbine but it can be a good approximation further North. Thus, the results from this model can give us a scale for the mean along shore velocities and the sea surface slope to compare with the numerical experiment outputs. If the wind forcing is uniform, the along shore variations can be neglected and the barotropic equations of motion with linear bottom friction become [*Brink,* 1998, *Csanady,* 1998], using the same notations as in the previous paragraph:

$$\frac{\partial \bar{u}}{\partial t} - f\bar{v} = \frac{\tau_x}{H\rho} - \frac{r\bar{u}}{H} \tag{2.5}$$

$$f\bar{u} = -g\frac{\partial \zeta}{\partial y} \tag{2.6}$$

$$\frac{\partial H\bar{v}}{\partial y} = 0 \tag{2.7}$$

The along shore velocities are forced by the along shore wind and the free surface remains in geostrophic equilibrium with the along shore velocities. In order to satisfy equation (2.7) and the fact that there is no cross-shore flow at the coastal boundary, the cross-shelf transport

has to vanish everywhere [*Brink,* 1998]. Starting from rest at t=0 with a constant wind stress, we obtain from equation (2.5):

$$\bar{u} = \frac{\tau_x}{\rho r}(1 - e^{-\frac{rt}{H}}) \tag{2.8}$$

If the maximum depth is 500 m, the solution is nearly stationary after 40 days with along shore velocities:

$$\bar{u} = \frac{\tau_x}{\rho r} \tag{2.9}$$

This result shows that bottom friction allows us to expect for the numerical experiments a steady solution after nearly 50 days with along shore velocities of the order of magnitude: $O(\frac{\tau_x}{\rho r})$, resulting from a balance between the wind stress and the bottom friction. For example if the wind stress value equal 0.1 N.m^{-2}, after 50 days the mean along shore velocities should be $O(0.33)$ m.s^{-1}.

2.4 The reference experiment

For the reference experiment, the constant wind stress value is fixed at $\tau = 0.1$ N.m^{-2} corresponding to the average wind stress measured in the area during upwelling seasons ($\tau \sim 0.098$ N.m^{-2}). The linear bottom friction coefficient value is r $= 3 \times 10^{-4}$ m.s^{-1} and the viscosity parameter is set to the lowest possible value to avoid numerical noise ($\nu_4 = 1.5 \times 10^9$ m^{4}s^{-1}).

Starting from rest, an equatorward current develops in response to the equatorward wind forcing. In balance with the along shore velocities, a cross shelf slope of the free surface is set up (figures 2.2-a, 2.2-b and 2.2-c). The solution becomes steady after 50 days (figure 2.2-c), the average sea surface slope value is between 0.17 and 0.38 centimeters per kilometer and the mean along shore velocities are approximately equal to 0.28 m.s^{-1}. Although the presence of a coastline and bottom topography variations induces a drag that reduces the along shore velocity, its value stays in the same order of magnitude as in the analytical solution. Four scaling parameters allow us to compare the results with other studies:

(1) the Rossby number,

$$Ro = \frac{\text{advection}}{\text{Coriolis}} = \frac{U}{fL}. \tag{2.10}$$

(2) Because of the use of a biharmonic operator, the Reynolds number takes the form:

$$Re_{biharm} = \frac{\text{advection}}{\text{viscosity}} = \frac{UL^3}{\nu_4} \tag{2.11}$$

(3) The Reynolds number associated with bottom friction,

$$Re_{friction} = \frac{\text{advection}}{\text{bottom friction}} = \frac{UH_0}{rL}, \tag{2.12}$$

which is equivalent to the 'island wake parameter' P introduced by Wolanski et al. [1984]. A scaling analysis shows that it is equivalent to the λ parameter defined by Becker [1991] (The same analysis shows that the lateral boundary layer thickness defined by Becker [1991] is in our case: $\delta = \frac{H^{\frac{1}{4}}\nu_4^{\frac{1}{4}}}{r^{\frac{1}{4}}L}$).

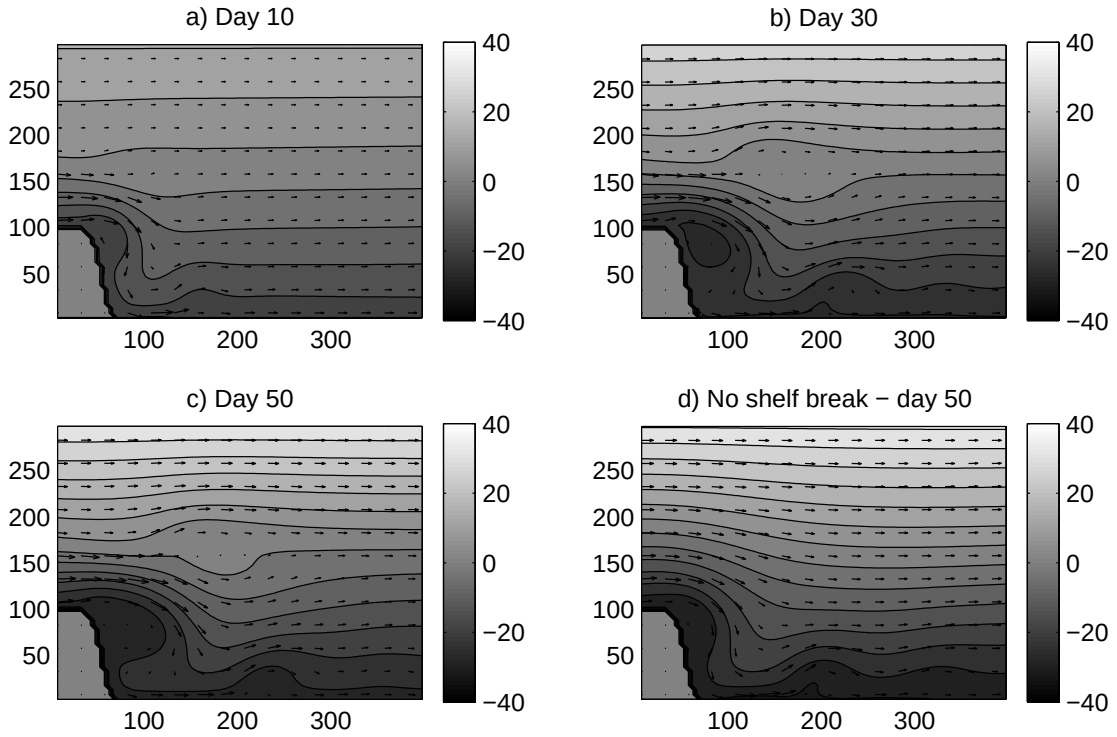

Figure 2.2 Barotropic velocities and free surface elevation for the reference experiment in the vicinity of Cape Columbine: a) day 10 (maximum velocity: 62 cm.s^{-1}, averaged velocity: 16 cm.s^{-1}), b) day 30 (maximum velocity: 69 cm.s^{-1}, averaged velocity: 25 cm.s^{-1}), c) day 50 (maximum velocity: 70 cm.s^{-1}, averaged velocity: 28 cm.s^{-1}),) d) day 50 for the same experiment with no shelf-edge (maximum velocity: 71 cm.s^{-1}, averaged velocity: 30 cm.s^{-1}). The horizontal coordinates are in kilometers and the greyscale range for the free surface elevation is in centimeters. The interval between the isolines is 5 cm.

(4) The Ekman number,

$$E_V = \frac{\text{bottom friction}}{\text{Coriolis}} = \frac{r}{fH_0}. \tag{2.13}$$

Where,

U is a characteristic velocity, $O(0.28)$ m.s^{-1}.

f is the Coriolis parameter, $-7.707 \times 10^{-5}\ s^{-1}$.

L is a characteristic length scale, for example the size of the cape: 100 km.

ν_4 is the viscosity parameter, $1.5 \times 10^9\ m^4.s^{-1}$.

H_0 is a characteristic depth, 150 m on the shelf.

r is the bottom friction parameter, $3 \times 10^{-4}\ m.s^{-1}$.

From these values we obtain: $Ro = 3.6 \times 10^{-2}$, $Re_{biharm} = 1.9 \times 10^5$, $Re_{friction} = 1.4$ and $E_V = 2.6 \times 10^{-2}$. Hence, Coriolis acceleration and the resultant pressure gradient are the main driving forces and at the first order, advection and bottom friction are the two important terms controlling the flow. Further, those terms show that this experiment is in the attached-cyclonic-eddy regime [small Rossby number, small Burger number (null in our case)] when the cape is on the left (in the Northern Hemisphere) of the study of Boyer and Tao [1987a]. $Re_{friction} = O(1)$ shows that this regime corresponds to the stable wake regime of Wolanski et al. [1984a]. $\lambda = 1.4$ and $\delta = 5.2 \times 10^{-2}$ are at the limit between the detachment and the no-detachment regime of Becker [1991, see figure 7]. The small Rossby and Ekman numbers correspond to the stable wake regime described by Boyer at al. [1987b, see figure 3].

The reference experiment shows that the bottom topography associated with Cape Columbine generates three main features:

(1) Attached cyclonic eddy: before day 10, the flow detaches from Cape Columbine and generates an attached cyclonic eddy (figure 2.2-a, x=50 km y=100 km). The size of the eddy is approximately 60 km at day 10 and expands to a size of 110 km by day 50 (figures 2.2-b and 2.2-c). The presence of this stationary attached-cyclonic-eddy is in agreement with the in-situ measurements of Holden [1985] and the recent averaged ADCP data of Boyd and Oberlholster [1994]. It can be compared with the schematic representation of the currents in St Helena Bay (figure 1.13) made by Shannon [1985]. This is also in agreement with the experimental results of Boyer and Tao [1987a] for the cape on the left (Northern Hemisphere), the smallest Burger number and $Ro = O(0.02)$. Further, the presence of the cyclone and the strength of the velocities match the results of the 3D model of Oey [1996, see figure 12 and figure 13]. In the Santa Barbara Channel model, which includes baroclinic processes, Oey [1996] applied an equatorward wind stress similar to the forcing of the reference experiment. The bottom fiction is quadratic ($C_d = 2.5 \times 10^{-3}$) and the grid resolution is 5/3 km. The equatorward flow associated with a pronounced coastal upwelling is comparable with the barotropic velocities obtained here, and forms a stationary cyclonic eddy in the lee of Point Conception. The size of this eddy is approximately half the size of our barotropic eddy. This discrepancy might be due to the depth of the shelf (300 m versus 150 m in our experiment), the width of the shelf (50 km versus 150 km in our experiment) or the presence of the Santa Barbara islands that might block the cyclone extension.

(2) Influence of the shelf break: the steep shelf edge offshore (figure 2-b, y=150 km) apply a strong topographic constraint on the flow, prohibiting cross-topographic currents. Thus, mass conservation implies that the velocities between Cape Columbine and the shelf break (figures 3-a, 3-b and 3-c, for x=0 km and y=0 to 150 km) are stronger than in the other parts of the shelf. This can affect the detachment process. An experiment with no shelf break (figure 2.2-d) shows that at day 50, the size of the cyclonic eddy is approximately 60 % the size of the eddy in the reference experiment. The value of the along shore velocities near the tip of the cape is 80 % the value of the velocities in the reference experiment. Further, vortex squashing produces an anticyclonic bend on the shelf edge (figure 2.2-c, x=180 km, y=150 km) and a divide in the currents (figure 2.2-c, x=110 km, y=150 km). Its location corresponds approximately to the location of the Columbine divide described by Shannon [1985a], and it can be an explanation of this phenomenon.

(3) Upstream blocking: the artificial cape on the right seems to have no influence on the detachment processes, but it produces weak near shore velocities on the right of the shelf (figure not shown). This effect can be felt up to 300 km [O(external Rossby radius of deformation)] upstream of the cape. Because we use a large domain (900 km along shore), this phenomenon does not affect our area of interest. This has been tested using a smaller domain (600 km along shore) and the similarities between the solutions validate the use of the periodic channel.

2.5 Diagnostic analysis

2.5.1 Dynamical balance

To understand the processes involved in the cyclone generation, the dynamical terms have been computed from the model outputs using equations (2.1) and (2.2). They have been rewritten in the form of a sum of acceleration vectors as follow:

$$\underbrace{\frac{1}{D}\frac{\partial D\vec{u}}{\partial t}}_{\overrightarrow{Tendency}} = \underbrace{-\frac{1}{D}[\nabla.(D\vec{u})]\vec{u}}_{\overrightarrow{Advection}} \underbrace{-f\vec{k}\wedge\vec{u}}_{\overrightarrow{Coriolis}} \underbrace{-g\nabla\zeta}_{\overrightarrow{GradP}} \underbrace{+\frac{\nu_4}{D}\hat{\triangle}\frac{\hat{\triangle}\vec{u}}{D}}_{\overrightarrow{Viscosity}} \underbrace{-\frac{r\vec{u}}{D}}_{\overrightarrow{Friction}} \underbrace{+\frac{\vec{\tau}}{\rho D}}_{\overrightarrow{Forcing}} \tag{2.14}$$

Where $\vec{u}$ is the vertically averaged flow velocity, $\vec{\tau}$ is the wind stress and $\vec{k}$ is a vertical unit vector. Because $\frac{\zeta}{H} \sim O(10^{-3}) \ll 1$ and $\frac{\frac{\partial D}{\partial x}}{D} \sim O(10^{-5}) \ll 1$, the terms of equation (2.14) are respectively equivalent to the terms of the vertically averaged momentum equation:

$$\underbrace{\frac{\partial\vec{u}}{\partial t}}_{\overrightarrow{Tendency}} = \underbrace{-(\vec{u}.\nabla)\vec{u}}_{\overrightarrow{Advection}} \underbrace{-f\vec{k}\wedge\vec{u}}_{\overrightarrow{Coriolis}} \underbrace{-g\nabla\zeta}_{\overrightarrow{GradP}} \underbrace{+\nu_4\nabla^4\vec{u}}_{\overrightarrow{Viscosity}} \underbrace{-\frac{r\vec{u}}{D}}_{\overrightarrow{Friction}} \underbrace{+\frac{\vec{\tau}}{\rho D}}_{\overrightarrow{Forcing}} \tag{2.15}$$

It appears (figure 2.3-a) that, at zero order, the balance between pressure gradient and Coriolis acceleration overwhelms the other accelerations. This is in agreement with the small Rossby and Ekman numbers found previously. The Coriolis acceleration pushes the flow offshore, creating an Ekman transport away from the coast, in agreement with the upwelling models. Because of mass conservation, this transport produces a down slope toward the coast

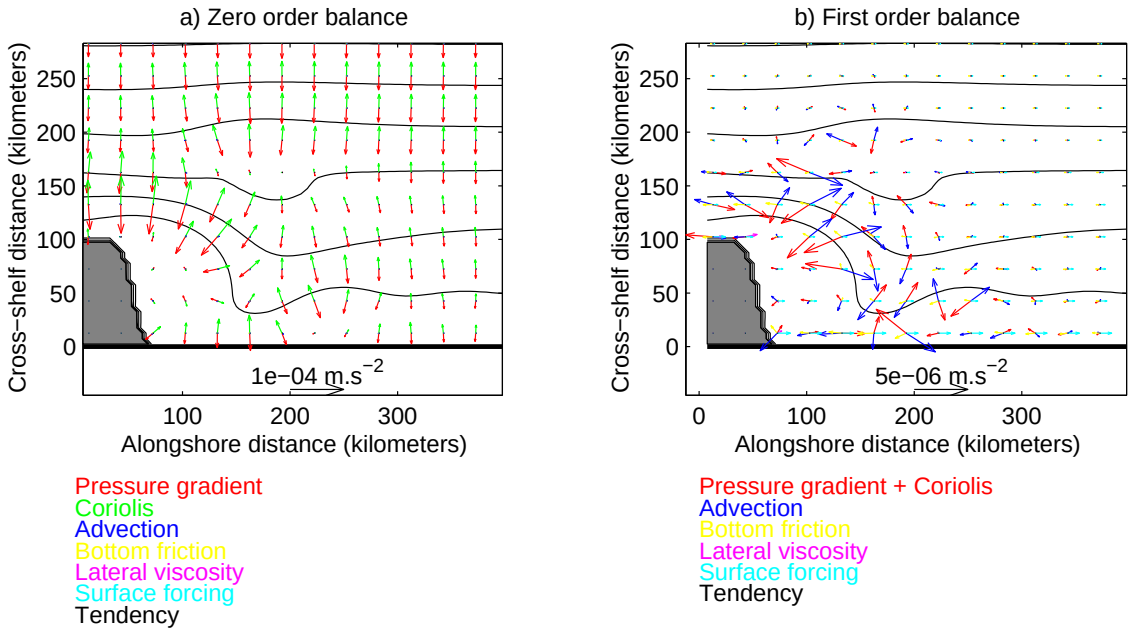

Figure 2.3 Accelerations (m.s^{-2}) applied to the water particles for the reference experiment at day 50 (the contours represent the free surface elevation). a) At zero order, the balance between pressure gradient and Coriolis acceleration dominates the dynamics. b) First order tendency terms: by summing the pressure gradient and the Coriolis acceleration vectors, the zero order balance can be filtered out and the first order terms can be studied. Note that this terms are 20 times smaller than the zero order ones.

in the free surface, generating a pressure gradient in balance with the Coriolis acceleration [*Csanady,* 1982].

By summing the pressure gradient and the Coriolis acceleration vectors, we can filter out the zero order balance and get the equilibrium at the first order [figure 2.3-b, note that these accelerations are 20 times smaller than in figure 2.3-a, in agreement with Ro and Ek $\sim O(10^{-2})$]. At this order, most of the terms start to be important. In the following, we call the sum of the pressure gradient and the Coriolis acceleration: the ageostrophic pressure gradient.

(1) Viscous terms are of an order of magnitude lower than the other ones. They have some relative importance near the tip of the cape (figure 2.3-b, x=40 km, y=100 km). As explained by Becker [1991], viscosity has to be small for detachment to occur.

(2) Around the external part of the eddy (figure 2.3-b, x=50 to 130 km, y=70 to 130 km), there is a competition between advection and ageostrophic pressure gradient. It appears that around the eddy (figure 2.3-b, x=140 km, y=100 km), the radius of curvature of the flow is approximately $R = 85$ km and the tangential velocities are about $V = 0.5$ m.s^{-1}. Then the normal acceleration is $\gamma = \frac{V^2}{R} \simeq 2.9 \times 10^{-6}$ m.s^{-2}, which is close to the value of the advective acceleration ($\simeq 3.4 \times 10^{-6}$ m.s^{-2}). This shows a cyclo-geostrophic equilibrium around the eddy. This advective acceleration, forcing the water particles away from the cape, seems to be responsible for the detachment.

(3) Away from perturbations (figure 2.3-b, for example y>220 km), the wind forcing and

bottom friction relative equilibrium controls the along shore velocities as in the analytical solution.

(4) Another equilibrium occurs where the velocities are weak: inside the eddy (figure 2.3-b, x=75 km, y=70 km) and in the upstream blocking area (x=650 to 850 km, y=0 to 60 km, figure not shown). In those places, the Coriolis acceleration is weak and a static wind stress-pressure gradient balance prevails.

2.5.2 Vorticity balance

To refine the study, curls of the acceleration vector fields extracted from equation (2.14) are computed to obtain the terms of the equation for the vertically averaged vertical component of vorticity, $\bar{\xi}$. Their physical meaning can be illustrated by deriving the curl of equation (2.15) and introducing the continuity equation (2.4):

$$\begin{aligned}
\underbrace{\frac{\partial \bar{\xi}}{\partial t}}_{\nabla\wedge\overrightarrow{Tendency}} = & \underbrace{-\bar{u}\frac{\partial \bar{\xi}}{\partial x} - \bar{v}\frac{\partial \bar{\xi}}{\partial y} + \frac{\bar{\xi}}{D}\left(\bar{u}\frac{\partial D}{\partial x} + \bar{v}\frac{\partial D}{\partial y} + \frac{\zeta}{\partial t}\right)}_{\nabla\wedge\overrightarrow{Advection}} \\
& \underbrace{+\frac{f}{D}\left(\bar{u}\frac{\partial D}{\partial x} + \bar{v}\frac{\partial D}{\partial y} + \frac{\zeta}{\partial t}\right)}_{\nabla\wedge\overrightarrow{Coriolis}} \\
& \underbrace{+\nu_4\left(\frac{\partial^4 \bar{\xi}}{\partial x^4} + \frac{\partial^4 \bar{\xi}}{\partial y^4}\right)}_{\nabla\wedge\overrightarrow{Viscosity}} \\
& \underbrace{-\frac{r\bar{\xi}}{D} + \frac{r}{D^2}\left(\bar{v}\frac{\partial D}{\partial x} - \bar{u}\frac{\partial D}{\partial y}\right)}_{\nabla\wedge\overrightarrow{Friction}} \\
& \underbrace{+\frac{1}{\rho D}\left(\frac{\partial \tau_y}{\partial x} - \frac{\partial \tau_x}{\partial y}\right) - \frac{1}{\rho D^2}\left(\tau_y\frac{\partial D}{\partial x} - \tau_x\frac{\partial D}{\partial y}\right)}_{\nabla\wedge\overrightarrow{Forcing}}
\end{aligned} \tag{2.16}$$

- $\nabla \wedge \overrightarrow{Advection}$ is the advection of vorticity added to the vortex stretching associated with relative vorticity.
- $\nabla \wedge \overrightarrow{Coriolis}$ is the vortex stretching associated with planetary vorticity. Because the Rossby number is small, this term is much larger (10 to 100 times) than the vortex stretching associated to relative vorticity.
- As explained by Signell and Geyer [1991], the first term of $\nabla \wedge \overrightarrow{Friction}$ is the vorticity dissipation by bottom friction, and the second one is the 'slope torque' which acts as a source of vorticity when there is a component of velocity normal to a depth gradient. These two terms are in the same order of magnitude. Because $Re_{friction} = O(1)$, the curl of bottom friction should be the same order of magnitude as the advection of vorticity.
- The first term of $\nabla \wedge \overrightarrow{Forcing}$ is the Ekman pumping associated with the wind stress curl and the second term is, by analogy with the 'friction slope torque', a 'wind stress

slope torque' which can be a source of vorticity when the wind is normal to a depth gradient. In our case, for $\tau_y = 0$ and $\tau_x = 0.1\ N.m^{-2}$, the order of magnitude of the ratio between 'wind stress slope torque' and advection of vorticity is:

$$\frac{\tau_x L}{\rho H_0 U^2} \sim 1.4 \tag{2.17}$$

This term can not be neglected. Its effects can be illustrated by traking the curl of the analytical solution for the velocities (equation 2.8). During the spin-up, because H is a function of y, $\bar{u}$ is also a function of y. Thus the vorticity is:

$$\begin{aligned} \bar{\xi} &= -\frac{\partial \bar{u}}{\partial y} \\ &= \frac{\tau_x \frac{\partial H}{\partial y}}{\rho H^2} e^{-\frac{rt}{H}} \end{aligned} \tag{2.18}$$

In this case, the vorticity produced continually from the beginning of the experiment by the 'wind stress slope torque', is progressively dissipated by bottom friction and 'friction slope torque'. Thus, after 50 days, the stationary solution is irrotational. In the same manner as the 'friction slope torque', the 'wind stress slope torque' appears because surface and bottom stresses have a stronger effect in shallow waters than in deep waters.

Figure (2.4) exhibits the relative importance of the vorticity equation terms in the vicinity of Cape Columbine. The advection of vorticity (figure 2.4-a) contains as well the vortex stretching associated to relative vorticity, but this term is one order of magnitude smaller than the other terms. The curl of bottom friction (figure 2.4-b) contains both the bottom dissipation and the 'friction slope torque' and is thus not proportional to relative vorticity in shallow waters. The vortex stretching (figure 2.4-c) is the vortex stretching associated to planetary vorticity. The unit of these terms is s^{-2} and for clarity the values have been multiplied by 10^{10} (figures 2.4-a, 2.4-b, 2.4-c, 2.4-d and 2.4-e). To validate the approximations made in deriving the tendency terms, the curl of the pressure gradient has been also portrayed, multiplied by 10^{24} (figure 2.4-f).

We can then extract a number of equilibriums:

(1) The balance between advection of vorticity and vortex stretching occurs almost everywhere where the slopes are strong: on the shelf break (figures 2.4-a and 2.4-c, y=150 to 200 km) and in the bay (figures 2.4-a and 2.4-c, y=0 to 60 km)

(2) Around the external part of the eddy, where the shelf is relatively flat and the dynamics are cyclo-geostrophic (see previous section), the curl of bottom friction balances the advection of vorticity (figures 2.4-a and 2.4-b, x=50 to 130 km, y=70 to 130 km). This balance seems to follow the contour of the eddy, and might control its extension.

(3) As pointed out in the previous section, the lateral viscosity has some importance near the tip of Cape Columbine. In figure 2.4-d, the viscous boundary layer is clearly seen for x=0 to 50 km and y=100 to 110 km. Past the cape, there is a detachment of this boundary layer (figure 2.4-d, x=50 to 80 km, y=115 km).

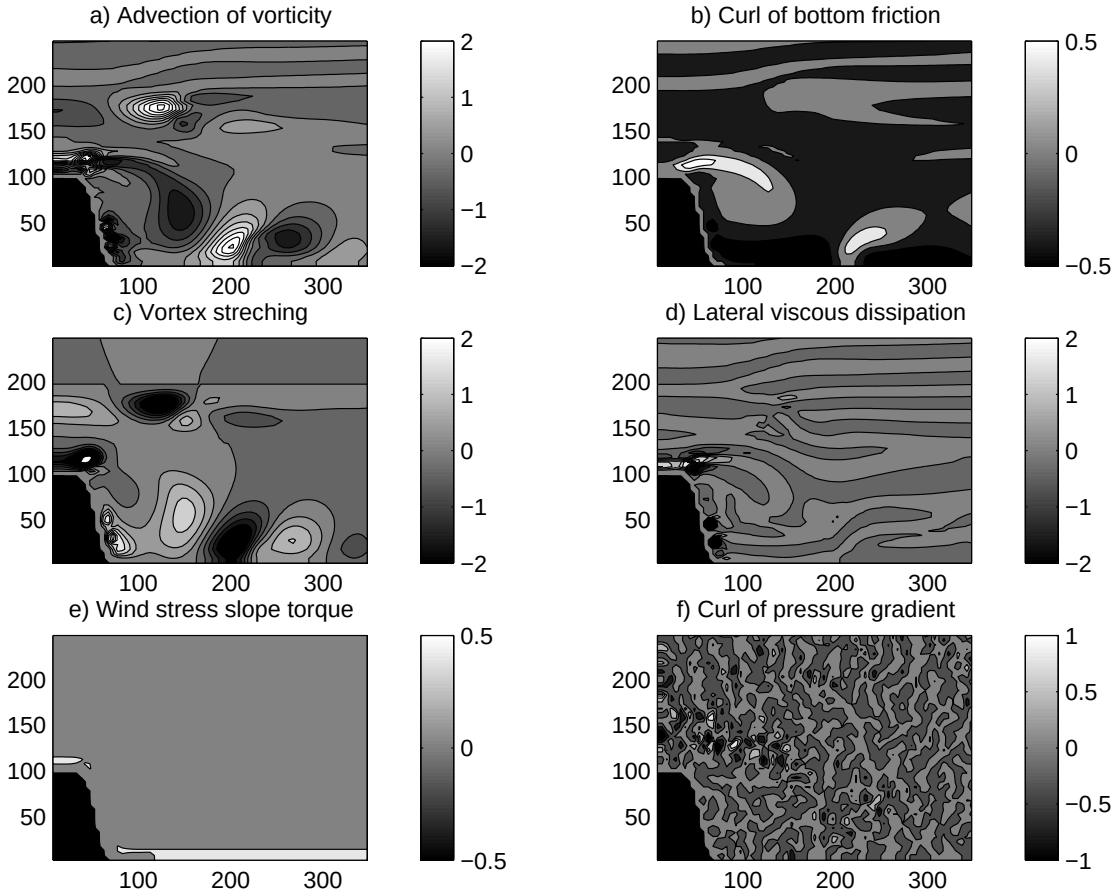

Figure 2.4 Tendency terms of the vorticity equation (s^{-2}), computed from the dynamical terms at day 50 for the reference experiment: a) advection of vorticity, b) curl of bottom friction, c) vortex stretching, d) lateral viscous dissipation, e) wind stress slope torque, f) curl of the pressure gradient. The horizontal coordinates are in kilometers and the greyscale range represents the values in s^{-2}, multiplied by 10^{-10}, except for the values of curl of the pressure gradient which are multiplied by 10^{-24} to show the validity of the computation.

(4) In shallow waters, the friction and wind stress slope torques start to have a strong influence and seem to be in balance for x>80 km and y=0 to 10 km (figures 2.4-b and 2.4-e).

We can expect from the second point that the size of the eddy is controlled by the balance between advection of vorticity and curl of bottom friction. From this, we can extract a characteristic length scale l:

$$\frac{H_0 U^2}{l^2} \text{ (advection of vorticity)} \sim \frac{rU}{l} \text{ (curl of bottom friction)} \tag{2.19}$$

$$\Rightarrow l \sim \frac{H_0 U}{r} \tag{2.20}$$

This length scale can be seen as a frictional e-folding distance and is equivalent to the eddy length scale R_l described by Pattiaratchi et al. [1986] and Wolanski et al. [1984]. It is also equivalent to the frictional length scale l_f tested by Signell and Geyer [1991].

Taking the analytical result (equation 2.9) for the characteristic velocities, the equation (2.20) becomes:

$$l \sim \frac{H_0 \tau}{\rho r^2} \tag{2.21}$$

That gives us a characteristic eddy length scale which is a function of the wind stress and of the linear bottom friction parameter. This length scale can be compared to the size of the eddy. In this example, $H_0 = 150$ m, $\frac{\tau}{\rho} = 10^{-4}$ m^2.s^{-2}, and $r = 3 \times 10^{-4}$ m.s^{-1} so that $l = 167$ km (the difference with the model outputs can be seen in figure 2.2).

2.6 Sensitivity tests

To test the effects of the surface wind stress, the bottom friction coefficient, the size of the cape, the grid resolution, the viscosity coefficient and the domain size on the recirculation process, several numerical experiments are conducted by varying one parameter at a time. Within realistic parameter values, the grid resolution and the viscosity do not have much effect on the cyclone generation. However, the nature of the cyclone does depend on bottom friction, wind and the size of the cape.

2.6.1 Influence of the wind stress

Using the same parameters as in the reference experiment, ten experiments are run with different along shore wind stress values, varying from 0.02 N.m^{-2} to 0.2 N.m^{-2}. These wind stress values correspond to wind velocities at 10 m elevation of about 4 m.s^{-1} to 11 m.s^{-1} .

In all cases, the solution is steady after 50 days and the order of magnitude of the mean velocities is in agreement with the analytical solution (figure 2.5). The characteristic velocities range from 0.05 m.s^{-1} to 0.4 m.s^{-1}. The associate scaling parameters are, using the same characteristic numbers as in section 2.4:

- $Ro \sim 6 \times 10^{-3}$ to 5.3×10^{-2}
- $Re_{biharm} \sim 3.1 \times 10^4$ to 2.7×10^5
- $Re_{friction} \sim 0.23$ to 2.1

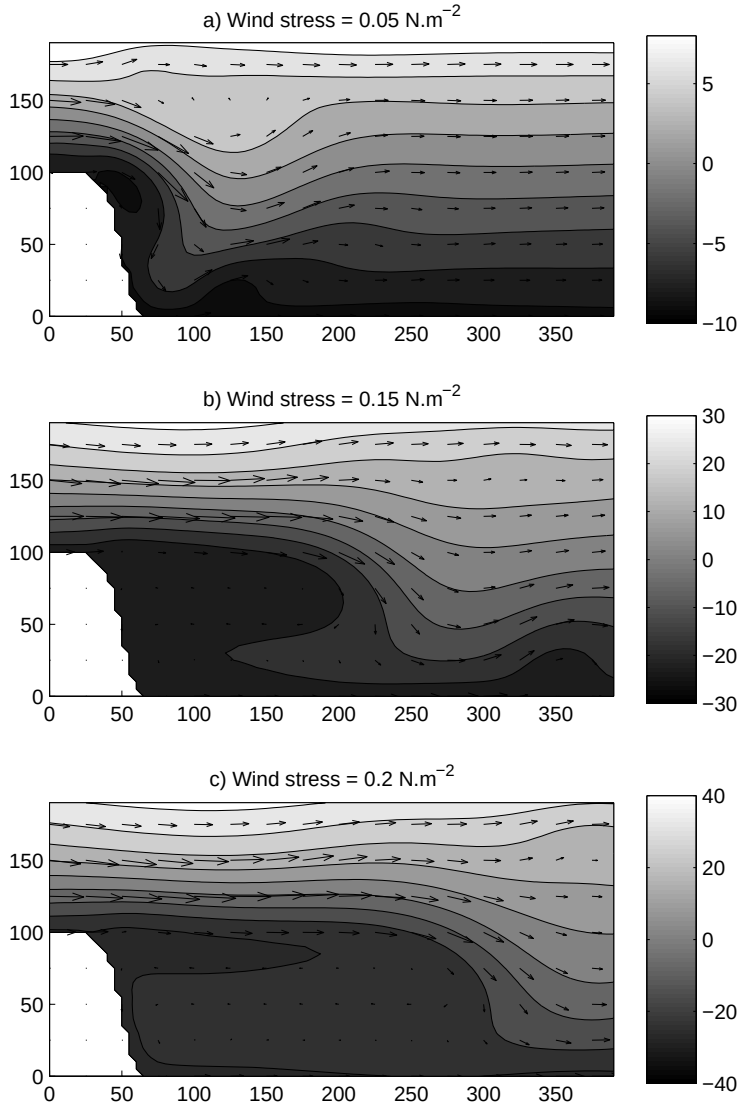

Figure 2.5 Barotropic velocities and sea surface elevation at day 100 for different values of the along shore wind stress. a) 0.05 $N.m^{-2}$ (maximum velocity: 38 cm.s^{-1}, averaged velocity: 12 cm.s^{-1}), b) 0.15 N.m^{-2} (maximum velocity: 100 cm.s^{-1}, averaged velocity: 36 cm.s^{-1}), c) 0.2 N.m^{-2} (maximum velocity: 130 cm.s^{-1}, averaged velocity: 46 cm.s^{-1}). The horizontal coordinates are in kilometers and the greyscale range for the free surface elevation is in centimeters. The interval between the isolines is 2 cm for (a), 6 cm for (b), and 8 cm for (c).

- $E_V = 2.6 \times 10^{-2}$ as in the reference experiment.

This corresponds to the same regime as for the reference experiment: small Rossby and Ekman numbers, large viscous Reynolds number and friction Reynolds number $\sim O(1)$. The results of Becker [1991] tell us that if $Re_{friction} < 1$ detachment should not occur, but the presence of bottom topography induces another detachment process, resulting from input of vorticity by vortex stretching, friction slope torque or wind stress slope torque. For example a detachment process can be explained by absolute vorticity conservation. If a water particle follows an isobath cyclonically bent with the coast on the left, like an equatorward current around Cape Columbine, it acquires cyclonic vorticity, $\xi < 0$. For the sake of absolute vorticity conservation ($\frac{f+\xi}{H} = cst.$), the particle is displaced offshore onto a deeper isobath (because here, $f < 0$). The particle needs a steeper turn to go back to the first isobath, hence stronger negative relative vorticity. This moves the particle into deeper waters and so on, and detachment occurs. This shows that the presence of bottom topography can favor detachment of the flow for an equatorward eastern boundary current past a cape. On the contrary, bottom topography can be a stabilization process for a poleward eastern boundary current. Hence, Becker's [1991] criterion does not apply in our case, and we still have detachment even for a small frictional Reynolds parameter (figure 2.5-a).

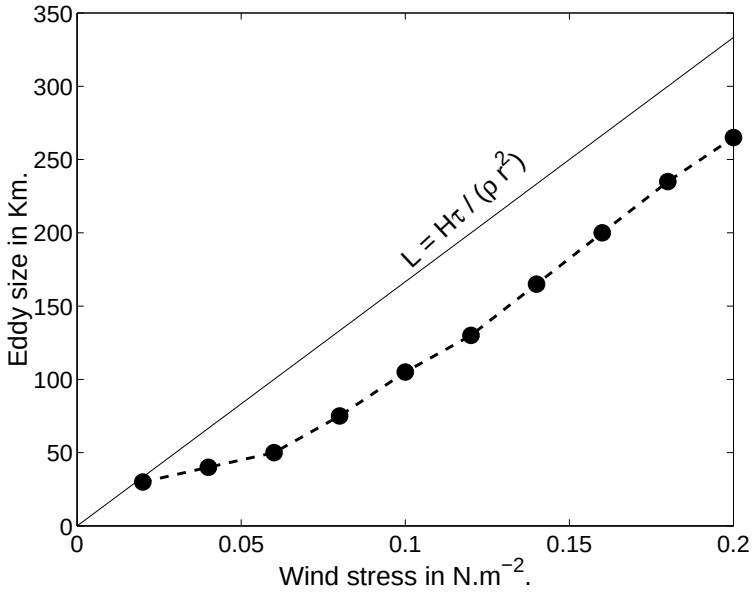

Figure 2.6 Along shore extension of the eddy at day 50 as a function of the wind stress. Comparison with the characteristic length scale: $l = \frac{H_0 \tau}{\rho r^2}$.

To characterize the size of the eddy as a function of wind stress, we choose to measure the distance between the tip of the cape and the place where the flow is the strongest towards the coast. The along shore eddy length given by this method is proportional to the wind stress (figure 2.6) and the trend is in agreement with the characteristic length scale found in section 6.2 (figure 2.5-a, 2.5-b, 2.5-c and 2.6). There is though an approximately constant discrepancy ($\sim$ 50 km) between the numerical results and the characteristic length scale, that reveals that something is missing in deriving the analytical length scale.

Within the eddy, the flow is weak and the along shore velocities are positive for $y < 20$ km and $y > 100$ km and negative around $y = 60$ km. The constant nature of this pattern might be related to the slope of the shelf or to the size of the cape.

2.6.2 Influence of the linear bottom friction coefficient

Ten more numerical experiments with wind stress fixed at 0.05 $N.m^{-2}$ were conducted to explore the effects of the linear bottom friction coefficient. This parameter varies from 0.5×10^{-4} m.s^{-1} to 5×10^{-4} m.s^{-1}. For low bottom friction values, the solution was not yet stationary at day 50, so day 100 is analyzed.

The mean velocities are again in the same order of magnitude as predicted by the analytical calculations (figure 2.7). As in the previous section, the different characteristic velocities and characteristic parameters are derived. For increasing r, they follow the range:

- $U \sim 0.5$ to $0.08\ m.s^{-1}$
- $Ro \sim 6 \times 10^{-2}$ to 10^{-3}
- $Re_{biharm} \sim 3 \times 10^5$ to 5×10^4
- $Re_{friction} \sim 15$ to 0.2
- $E_V = 4.3 \times 10^{-3}$ to 4.3×10^{-2}.

Again the Rossby and Ekman numbers are small and the viscous Reynolds number is very large. But for this set of experiments, the frictional Reynolds number which is the most important in the control of the detachment process, varies through two orders of magnitude. Because this number is equivalent to the island wake parameter of Wolanski et al. [1984], we can expect a domination of bottom friction for low values and instabilities for large values. For low bottom friction, the along shore size of the eddy does not match the characteristic length scale and three small eddy cells keep on moving inside a global structure(figure 2.7-a). The solution is not yet steady at day 100 and different dynamical balances should exist. It appears that in this experiment, we are in a eddy shedding regime.

For $r > 10^{-4}$ m.s^{-1} and corresponding $Re_{friction} < 7.5$, the eddy size does scale with r^{-2} (figure 2.8), but as in the previous section this size is not in agreement with the characteristic length scale.

This analysis confirms the key role of bottom friction in controlling the detachment processes and the importance of parameterizing it carefully.

2.6.3 Influence of the size of the cape

To explore the influence of the size of the cape on the detachment process, a set of experiments has been conducted with a size of the cape ranging from 25 km to 150 km and a wind stress ranging from 0.025 N.m^{-2} to 0.2 N.m^{-2}. The cross-shelf width of the periodical channel has been extended up to 300 km in order to contain the biggest capes. The bathymetry has been computed in such a way that the distance between the tip of the capes and the shelf break remains identical between all the experiments. This implies that the width of the shelf in the bay varies with the size of the cape (figure 2.9). The other parameters remain identical to the reference experiment.

In every case, the solution is stationary after 50 days and remains in the attached cyclonic eddy regime. The free surface elevation and the currents at day 100 for a wind stress of 0.1 N.m^{-2} reveal large differences depending on the size of the cape (figure 2.10):

(1) In the bay, the drag induced by the presence of the cape produces an averaged weaker current as the size of the cape increases. This averaged velocity ranges from 32 cm.s^{-1} for a cape of 25 km to 22 cm.s^{-1} for a cape of 50 km (for a wind stress of 0.1 N.m^{-2}).

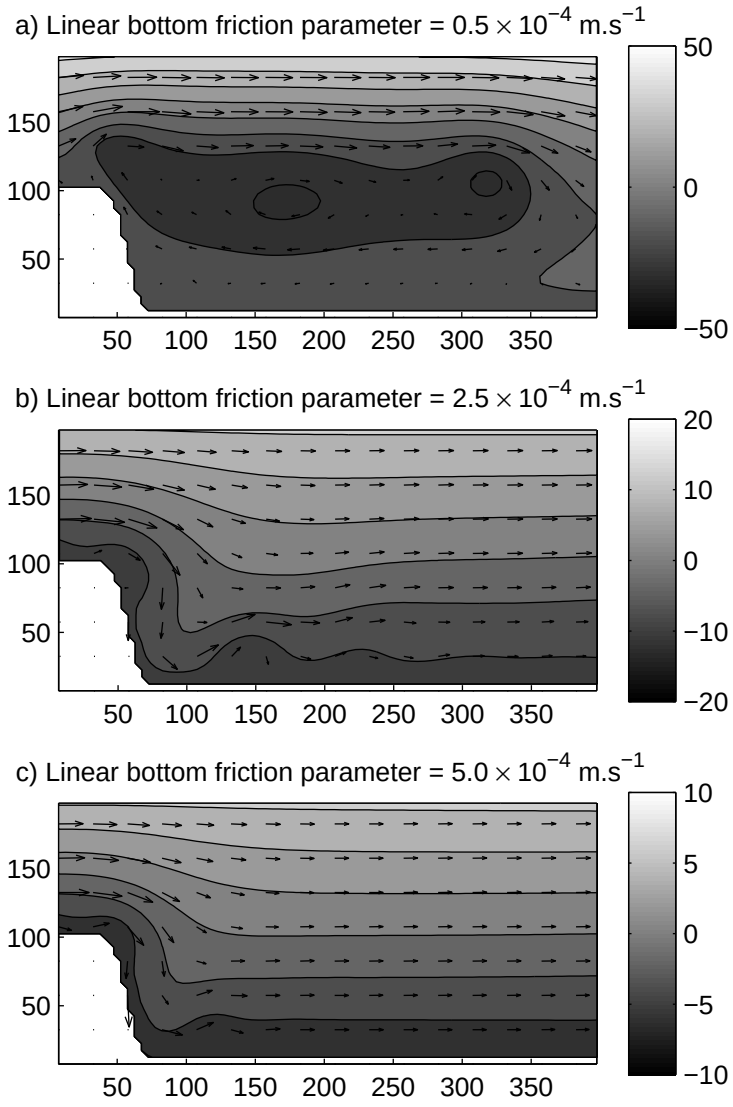

Figure 2.7 Barotropic velocities and sea surface elevation at day 100 forced by a constant wind stress (0.05 N.m^{-2}), for different values of the linear bottom coefficient r: a) $r = 0.5 \times 10^{-4}$ m.s^{-1} (maximum velocity: 129 cm.s^{-1}, averaged velocity: 49 cm.s^{-1}), b) $r = 2.5 \times 10^{-4}$ m.s^{-1} (maximum velocity: 35 cm.s^{-1}, averaged velocity: 14 cm.s^{-1}), c) $r = 5.0 \times 10^{-4}$ m.s^{-1} (maximum velocity: 19 cm.s^{-1}, averaged velocity: 8 cm.s^{-1}). The horizontal coordinates are in kilometers and the greyscale range for the free surface elevation is in centimeters. The interval between the isolines is 10 cm for (a), 4 cm for (b), and 2 cm for (c).

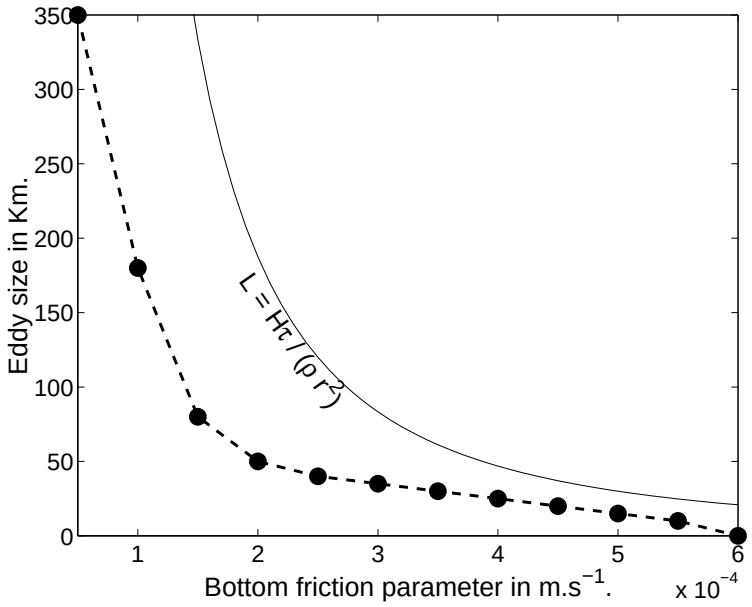

Figure 2.8 Along shore extension of the eddy at day 100 as a function of the linear bottom friction parameter r. Comparison with the characteristic length scale: $l = \frac{H_0 \tau}{\rho r^2}$.

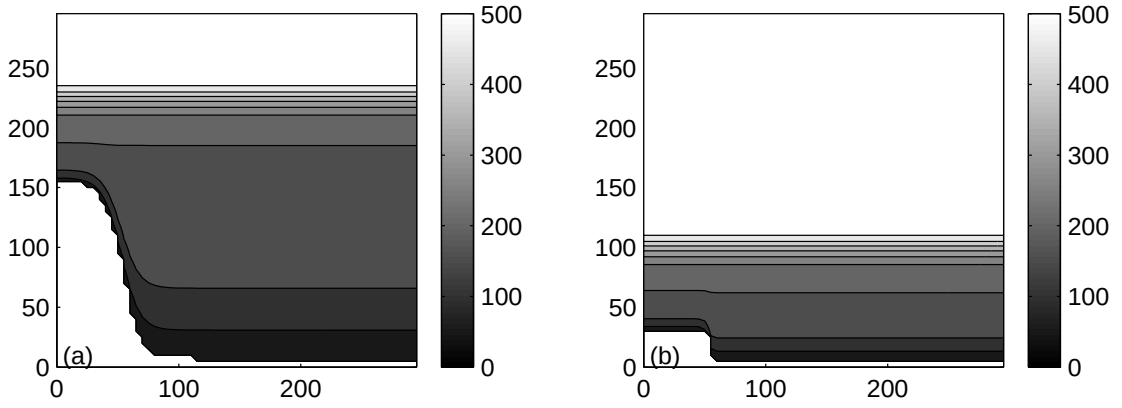

Figure 2.9 Bottom topography implemented in the model for (a) a cape of 150 km and (b) a cape of 25 km. The horizontal coordinates are in kilometers. The depths scale is in meters.

(2) The shelf break acting as an offshore barrier, mass conservation implies a stronger current at the tip of the cape for a larger cape than for smaller ones. The velocities at the tip of the cape range from 56 cm.s^{-1} for a cape of 25 km to 80 cm.s^{-1} for a cape of 150 km (for a wind stress of 0.1 N.m^{-2}).

(3) These large differences in velocity, imply that a scaling of the eddy length only dependent on the wind stress is no longer valid: large variations in the size of the eddy depends on the size of the cape (see figure 2.10 and figure 2.11).

The difference between the size of the eddy and the frictional characteristic length scale increases when the size of the cape decreases (figure 2.11). The balance advection / bottom friction is less valid for small capes. This can be explained by the reduction of the importance of the flat area in the lee of the cape for small capes (zero for a cape of 25 km, see figure 2.9). Because the sloping areas are relatively more important, the vortex stretching term gain importance relative to the bottom friction term when the size of the cape decreases. For a cape of 25 km, the size of the eddy as a function of the wind stress follows a totally different trend than for the other experiments. For large capes (> 100 km), the characteristic length scale gives a good approximation for the size of the eddy as a function of the wind stress.

The size of the cape affects dramatically the recirculation patterns in the bay. The length scale derived in section (2.5.2) does not take the size of the cape into account. Hence, further investigations will be necessary to improve the understanding of the circulation in the bay.

2.7 An upwelling plume ?

In section 1.4.4, it has been emphasized that a characteristic pattern in St. Helena Bay is the development of an upwelling plume from the tip of Cape Columbine. Numerous studies have been conducted to explain the presence of this upwelling plume due to the cyclonic wind stress curl measured in the lee of the cape [*Jury,* 1985a, *Jury,* 1985b, *Jury,* 1988, *Kamstra,* 1985, *Taunton-Clark,* 1985]. Although cyclonic wind stress curl might be important in this area, and locally enhances upwelling, none of these studies were able to model or quantify the impact of wing stress curl on the upwelling structure. This has been done, using a one and a half layer reduced-gravity model for the upwelling of Point Arena on the US West Coast by Enriquez and Friehe [1995]. Although their model produced an enhanced upwelling due to the presence of cyclonic wind stress curl, it didn't generate a marked upwelling plume extending from the cape.

In this section, I would like to propose the 'barotropic coastal flow detachment' as another possible process for the generation of the Cape Columbine upwelling plume. To illustrate this hypothesis, a 'barotropic' tracer has been introduced in the model to roughly simulate the sea surface temperature. It follows an advection equation:

$$\frac{\partial T}{\partial t} + \bar{u}\frac{\partial T}{\partial x} + \bar{v}\frac{\partial T}{\partial y} = 0 \tag{2.22}$$

To avoid the generation of numerical noise, biharmonic viscosity has been added. At the model initialization, the value of the tracer is 20 everywhere, except on a narrow band of 10 km at the tip of the Cape (x < 30 km, y =110 km) where it has a value of 10, accounting for the coastal upwelling. During all the simulation, the tracer is nudged towards 10 in this band. Although the offshore Ekman drift is not taken into account, this experiment is performed to simulate the characteristic sea surface temperature pattern observed in St Helena Bay.

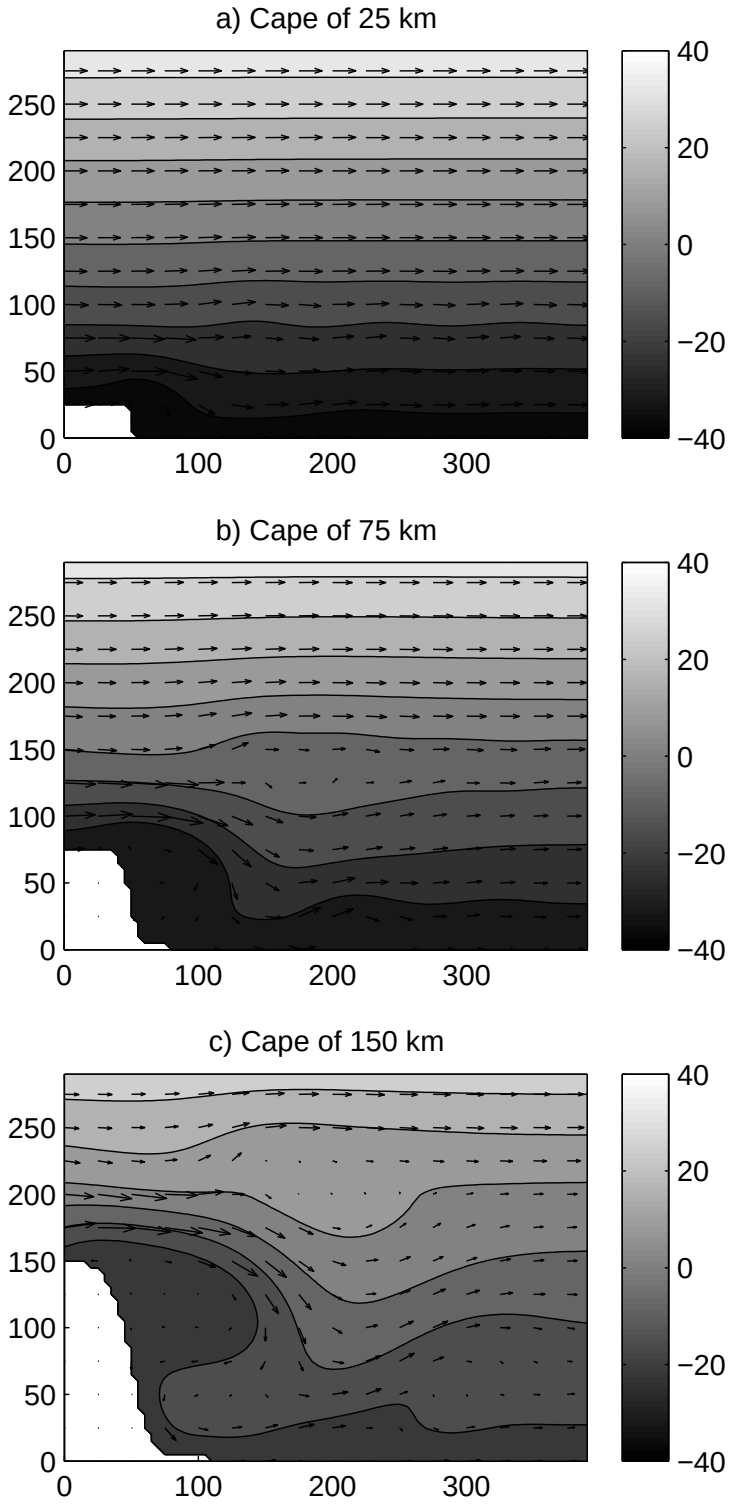

Figure 2.10 Barotropic velocities and sea surface elevation at day 100 forced by a constant wind stress (0.1 $N.m^{-2}$), for different sizes of the cape. a) Cape of 25 km (maximum velocity: 56 $cm.s^{-1}$, averaged velocity: 32 $cm.s^{-1}$). b) Cape of 75 km (maximum velocity: 68 $cm.s^{-1}$, averaged velocity: 29 $cm.s^{-1}$). c) Cape of 150 km (maximum velocity: 80 $cm.s^{-1}$, averaged velocity: 22 $cm.s^{-1}$). The horizontal coordinates are in kilometers and the greyscale range for the free surface elevation is in centimeters. The interval between the isolines is 8 cm.

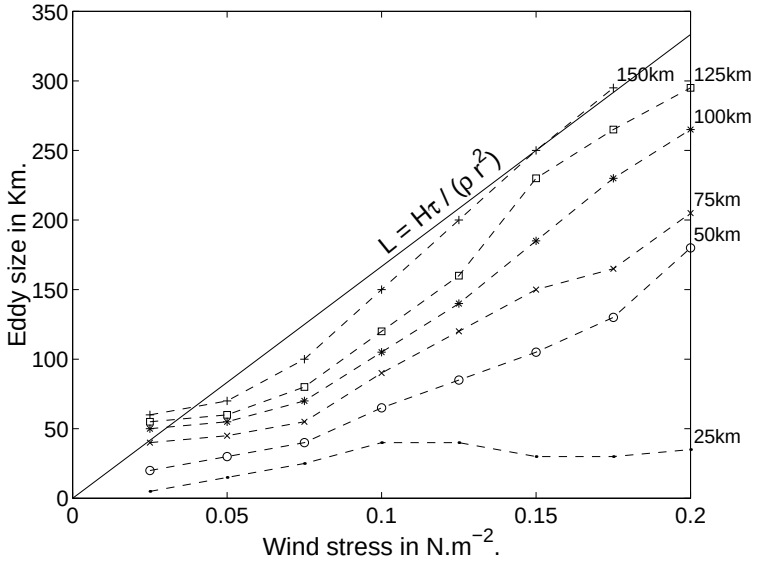

Figure 2.11 Size of the attached cyclonic eddy as a function of the wind stress and the size of the cape.

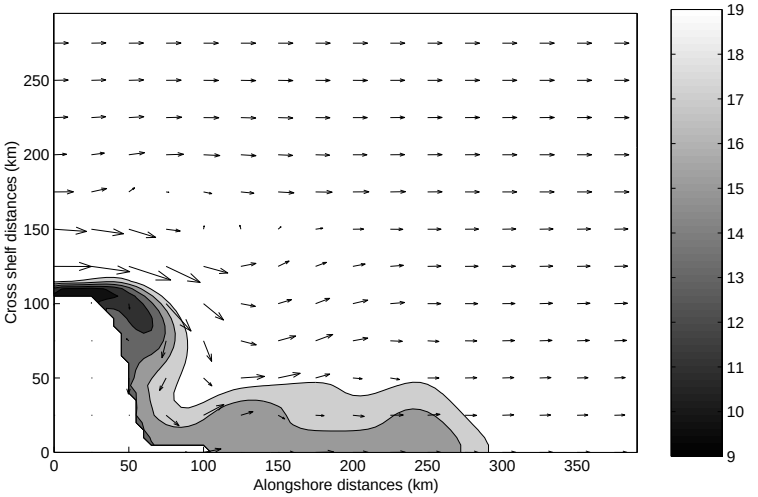

Figure 2.12 'SST' tracer after 30 days in a experiment forced by a wind stress of 0.05 N.m^{-2}. The advection of low values of the tracer by the detached flow simulate the Cape Columbine upwelling plume. The interval between the isolines is 2.

The tracer has been tested in a simulation forced by a constant wind stress of 0.05 N.m^{-2}, the other parameters remaining as in the reference experiment. After 30 days, even with this low wind forcing, a tongue of low 'SST' extends from the tip of the cape following the cyclonic eddy (figure 2.12). The shape of this tongue can be compared to a sea surface portrayal of the Cape Columbine upwelling plume (figure 1.10). Thus, the horizontal advection of water upwelled South of Cape Columbine around the attached cyclonic eddy can be an explanation of the development of the Cape Columbine upwelling plume. Wind stress curl is not necessary for the generation of this plume.

Another interesting feature is the patch of low tracer value at the coast at 120 km downstream from the cape (figure 2.12). This seems to be related to wave like features visible in the currents downstream of the main perturbation. Perhaps, there is here a possible explanation for the presence of the Hondeklip Bay upwelling center.

2.8 Standing coastal trapped waves in the lee of Cape Columbine

The discrepancies between the characteristic length scale and the size of the eddy shown on figure (2.11) suggest that a balance between advection and bottom friction is not enough to describe the flow patterns in the Bay. Other processes may also contribute actively. Two indications reveal that the circulation observed in the lee of the cape might be related to standing coastal trapped waves. Firstly, a wave-like pattern can be seen along the coast, downstream of the cape (figure 2.2 for x > 200 km). Secondly, if we reverse the forcing and the topography orientation (i.e. for a poleward eastern boundary current, figure 2.13), there is no more detachment of the flow. This dissymetry is characteristic of a poleward propagating process that can create a standing perturbation if it is advected by a mean equatorward flow. Two candidates correspond to the 'poleward propagation along a coastal eastern boundary' requirement: Kelvin waves and coastal trapped waves.

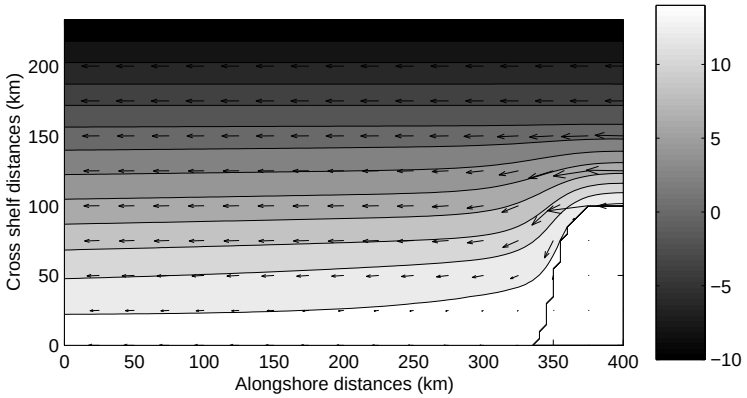

Figure 2.13 Barotropic velocities and free surface elevation at day 100 for a 'reversed' experiment where the wind stress of 0.05 N.m^{-2} is poleward. The topography orientation is also reversed. The maximum velocity is 38.5 cm.s^{-1} and the averaged velocity is 14 cm.s^{-1}. The horizontal coordinates are in kilometers and the greyscale range for the free surface elevation is in centimeters. The interval between the isolines is 2 cm.

2.8.1 Brief review on coastal trapped waves

For the last three decades, coastal trapped waves have been studied intensively. Buchwald and Adams [1968], derived the linear barotropic equation of motion on a f plane for along shore propagating waves. The variation of topography being of importance across the shelf, they kept the non-linear terms in the vertically integrated equation of continuity. Because they were looking for phenomena with spatial scales much smaller than the external radius of deformation, the rigid lid approximation was made. In this case, the cross-shelf structure of along shore propagating waves on an exponential topography follows a linear second order differential equation. In the Northern hemisphere, those free waves only propagate keeping the coast on their right (on their left in the southern hemisphere). The generation of these waves by atmospheric forcing has been analyzed by Gill and Schumann [1974] and they found that resonance can occur with propagating wind perturbations. By keeping the horizontal divergence, Huthnance [1975], derived 3 different kinds of barotropic trapped waves over the continental shelf: the Kelvin waves that propagate at the speed of long gravity waves, the edge waves with frequencies higher than f, and the coastal trapped waves of sub inertial frequencies. It happened that whereas edge waves may travel along the shelf in either direction, Kelvin and coastal trapped waves progress along the shelf in a cyclonic sense about the deep sea. There is a frequency at which the group velocity of coastal trapped waves vanishes. At this frequency, the wave energy cannot propagate along the shelf [*Huthnance,* 1975]. By including stratification, Huthnance [1978] showed analytically and numerically that the coastal trapped wave frequency increases with the measure of stratification. For weak stratification (small Burger number), these waves take the form of barotropic continental shelf waves, whereas for large stratification they take the form of internal Kelvin waves. For large along shore wavenumbers they take the form of bottom-trapped waves.

The presence of a mean along shore flow can alter considerably the free wave properties by Doppler shifting and change in the background vorticity [*Brink,* 1991, *Huthnance,* 1981]. Martell and Allen [1979] have studied the generation of continental shelf waves by small along shore variations in bottom topography. They used a perturbation method and found that shelf waves can be forced by the interaction of a wind stress forced current with small topographic disturbances. The advective effects of the unperturbed velocities are of importance, and lee waves form when their phase velocity opposes the advective velocities. The generation of lee waves is accompanied by a drag on the topographic obstacle. The influence of the presence of a cape in scattering coastal trapped waves has been explored analytically in the barotropic case [*Wilkin and Chapman,* 1987] and numerically when stratification has been included [*Wilkin and Chapman,* 1990]. In the barotropic case, reflection occurs when a wave encounters a narrowing shelf. When the shelf widens, the energy is transfered into higher modes and a shadow zone of very weak currents is present in the vicinity of the cape. Its extent increases with the size of the cape and decreases as the inverse of the wave frequency [*Wilkin and Chapman,* 1987]. When stratification is added, scattering is found to be amplified and intensification of the flow occurs within the scattering region [*Wilkin and Chapman,* 1990]. The influence of the advection by a mean current has not been taken into account in these last studies.

Coastal trapped waves have been observed along the coast of South Africa from tide gauges and current meters measurements. They propagate at a celerity ranging from 4.2 $m.s^{-1}$ to 6.7 $m.s^{-1}$. They induce variations in sea level up to 50 cm and strong current reversals along the South Coast. The Agulhas current damps dramatically wave propagation in the South-East [*Schumann and Brink,* 1990]. Large scale stationary features of the Benguela front observed

from satellite imagery have been related to the existence of barotropic shelf waves; but their standing nature has not been explained [*Shannon,* 1985].

The ingredients for standing lee shelf waves generation are present in the barotropic numerical experiments conducted in this chapter. The wave guide is formed by the shelf and the shelf edge slopes, the interactions between the wind forced current and Cape Columbine can provide the forcing mechanism, and the mean equatorward current allows the presence of a standing solution. Hence, the recirculation process in the lee of Cape Columbine could be related to the presence of lee shelf waves.

2.8.2 Wave lengths selected by a mean along shore current

The problem can be summarized has follow: what are the effects of the interactions between a large cape like Cape Columbine and a mean wind forced along shore current, on the circulation on the shelf in the lee of the cape ? The interactions between a cape and a mean along shore current of constant velocity U_0 are approximately equivalent to the interactions between a cape that moves in the opposite direction (with a velocity $-U_0$) and a fluid at rest. If (x, y, z, t) are the Eulerian coordinates in the fix referential and (x_1, y_1, z_1, t_1) are the coordinates in the referential attached to the moving cape, the temporal derivations have to be rewritten in the moving frame:

$$\frac{\partial}{\partial t} = \frac{\partial}{\partial x_1}\underbrace{\frac{\partial x_1}{\partial t}}_{U_0} + \frac{\partial}{\partial t_1} \tag{2.23}$$

For an observer moving with the cape, in the absence of wind stress, the vertically averaged momentum equation (2.15) and the continuity equation (2.4) take the form (removing the subscripts for the coordinates):

$$\begin{aligned} \frac{\partial \vec{u}}{\partial t} + U_0\frac{\partial \vec{u}}{\partial x} + (\vec{u}.\nabla)\vec{u} + f\vec{k}\wedge\vec{u} &= -g\nabla\zeta + \nu_4\nabla^4\vec{u} - \frac{r\vec{u}}{D} \\ \nabla(D\vec{u}) + \frac{\partial \zeta}{\partial t} + U_0\frac{\partial \zeta}{\partial x} &= 0 \end{aligned} \tag{2.24}$$

With the variables $\{x, y, t, D, \vec{u}, \zeta\}$ made dimensionless by the characteristic values defined in section (2.4) $\left\{L, L, T, H_0, U, U, \frac{fUL}{g}\right\}$ (T is a characteristic time scale, ~ 50 days), equations (2.24) leads to:

$$\begin{aligned} \frac{1}{fT}\frac{\partial \vec{u}}{\partial t} + \frac{U_0R_0}{U}\frac{\partial \vec{u}}{\partial x} + R_0(\vec{u}.\nabla)\vec{u} + \vec{k}\wedge\vec{u} &= -\nabla\zeta + E_H\nabla^4\vec{u} - \frac{E_v}{H + \frac{R_0L^2}{\mathcal{R}^2}\zeta}\vec{u} \\ \nabla\left[\left(H + \frac{R_0L^2}{\mathcal{R}^2}\zeta\right)\vec{u}\right] + \frac{1}{fT}\frac{L^2}{\mathcal{R}^2}\frac{\partial \zeta}{\partial t} + \frac{U_0R_0}{U}\frac{L^2}{\mathcal{R}^2}\frac{\partial \zeta}{\partial x} &= 0 \end{aligned} \tag{2.25}$$

where R_0 and E_V are the Rossby and the vertical Ekman numbers defined in section (2.4), $E_H = \frac{\nu_4}{fL^4}$ is the horizontal Ekman number associated to the biharmonic operator, and $\mathcal{R} = \frac{\sqrt{gH}}{f}$ is the external Rossby radius of deformation. In the regime of parameters of the reference experiment (section 2.4), fT, R_0, E_V and E_H are small compared to 1. $\mathcal{R} \sim 400$ km is greater than the characteristic length scale $O(100$ km$)$ of our problem, allowing the use of the rigid lid approximation. Although no constraint is given on the value of U_0 in

comparison to U, equations (2.25) are linearized keeping the term of advection of momentum by U_0. Hence the dimensional remaining equations of motion are:

$$\begin{aligned} U_0 \frac{\partial \vec{u}}{\partial x} + f\vec{k} \wedge \vec{u} &= -g\nabla\zeta \\ \nabla\left(H\vec{u}\right) &= 0 \end{aligned} \tag{2.26}$$

Equations (2.26) show that we are looking for a standing process looking from the point of view of a moving cape. The resulting vorticity equation takes the form:

$$U_0 \frac{\partial \bar{\xi}}{\partial x} = f\vec{u}.\frac{\nabla H}{H} \tag{2.27}$$

where the vortex stretching balances the advection of vorticity due to the displacement of the frame. Because bottom topography is defined in the fixed referential, it does not make sense that variations of bottom topography move from the cape point of view. Hence, H must not be variable in the along shore direction. Equation (2.27) becomes:

$$U_0 \frac{\partial \bar{\xi}}{\partial x} = f\bar{v}\frac{H'}{H} \tag{2.28}$$

The continuity equation in (2.26) is not divergent for the transport and allows us to define a transport stream function of the form:

$$H\bar{u} = -\frac{\partial \psi}{\partial y} \tag{2.29}$$

$$H\bar{v} = \frac{\partial \psi}{\partial x} \tag{2.30}$$

Introducing the transport stream function into the vorticity equation (2.28) yields to:

$$U_0 \frac{\partial}{\partial x}\left(\frac{\partial^2\psi}{\partial x^2} + \frac{\partial^2\psi}{\partial y^2}\right) - \frac{H'}{H}\left(U_0 \frac{\partial^2\psi}{\partial x \partial y} + f\frac{\partial \psi}{\partial x}\right) = 0 \tag{2.31}$$

The vorticity equation (2.31) can be linearized as done by Wilkin and Chapman [1987] by using a bathymetry that follows an exponential function:

$$H = H_{max}\, e^{-2\lambda(Y_{max}-y)} \tag{2.32}$$

Where Y_{max} is the position of the offshore boundary. This gives:

$$U_0 \frac{\partial}{\partial x}\left(\frac{\partial^2\psi}{\partial x^2} + \frac{\partial^2\psi}{\partial y^2}\right) - 2\lambda\left(U_0 \frac{\partial^2\psi}{\partial x \partial y} + f\frac{\partial \psi}{\partial x}\right) = 0 \tag{2.33}$$

Equation (2.33) accepts solutions in the form of standing shelf waves:

$$\psi = \psi_0 e^{ikx}\phi(y) \tag{2.34}$$

Introducing the wave solution (2.34) into (2.33) gives for $k \neq 0$:

$$\phi'' - 2\lambda\phi' - \left(k^2 + \frac{2\lambda f}{U_0}\right)\phi = 0 \tag{2.35}$$

As in section (2.2) an the analysis of Wilkin and Chapman [1987], we will suppose that the offshore boundary is closed by a wall at $y = Y_{max}$. It has been demonstrated that the presence of a wall at the shelf edge does not affect dramatically the shelf wave structure and dispersion relation [*Wilkin and Chapman,* 1987]. For the sake of mass conservation, ψ must be constant along the walls in y=0 and $y = Y_{max}$. For $k \neq 0$, this is only possible if $\phi(0) = \phi(Y_{max}) = 0$. This implies that the standing shelf waves do not produce any net transport. The solution for equation (2.35) that satisfies these boundary conditions is:

$$\phi = e^{\lambda y} sin\left(\frac{n\pi y}{Y_{max}}\right) \; ; \; n = 1, 2, 3, ... \tag{2.36}$$

Introducing the solution (2.36) into equation (2.35) selects an along shore wavenumber for each mode in the form:

$$k_n^2 = -\frac{n^2\pi^2}{Y_{max}^2} - \lambda^2 - \frac{2\lambda f}{U_0} \tag{2.37}$$

The full solution of the vorticity equation (2.33) can be write in the form of a sum of standing waves:

$$\psi_w(x, y) = \sum_{n=1}^{\infty} A_n e^{\lambda y} sin\left(\frac{n\pi y}{Y_{max}}\right) e^{ik_n x} \tag{2.38}$$

In the Southern Hemisphere, the Coriolis parameter f is negative. Thus, equation (2.37) implies that lee shelf waves can form only for positive U_0, accounting for an equatorward eastern boundary current. A more general condition for the presence of a lee shelf wave of mode n is:

$$0 < U_0 < \frac{2\lambda|f|}{\frac{n^2\pi^2}{Y_{max}^2} + \lambda^2} \tag{2.39}$$

If the relation (2.39) is not satisfied, k_n is imaginary and the wave is evanescent. For $n > \frac{Y_{max}}{\pi}\sqrt{-\lambda^2 - \frac{2\lambda f}{U_0}}$ only evanescent waves can be generated. Following Lighthill [1966], lee waves produced by a moving perturbation have to propagate at a phase velocity equal to the speed of the perturbation. Taking the propagating wave solution of Wilkin and Chapman [1987], we obtain $-U_0 = c_\phi = \frac{2\lambda f}{k_n^2 + \lambda^2 + \frac{n^2\pi^2}{Y_{max}^2}}$, which is identical to equation (2.37). The condition (2.39) says that standing lee shelf wave can only exist if U_0 is opposite to the shelf wave propagation and smaller than the fastest shelf wave phase celerity.

Following the same approach of the section (2.5.2) , the wind forced characteristic velocity defined by equation (2.9) can give a reasonable value for U_0 in equation (2.37). We obtain a standing shelf wave length L_n for each mode as a function of the wind stress:

$$L_n = \frac{2\pi}{\sqrt{-\frac{n^2\pi^2}{Y_{max}^2} - \lambda^2 - \frac{2\lambda f \rho r}{\tau}}} \; ; \; n = 1, 2, 3, ... \tag{2.40}$$

To compare this result to the outputs from the previous experiments, the topographic parameters have been chosen: $\lambda = 7 \times 10^{-6}$, $Y_{max} = 180$ km and $H_{max} = 500$ m, so that the exponential topography is relatively close to the bathymetry of the numerical model in St. Helena Bay (2.2) (figure 2.14).

The wavelengths of the first two modes are of the same order of magnitude as the size of the perturbations observed in the lee of the cape (for a cape of 100 km)(figure 2.15). Thus

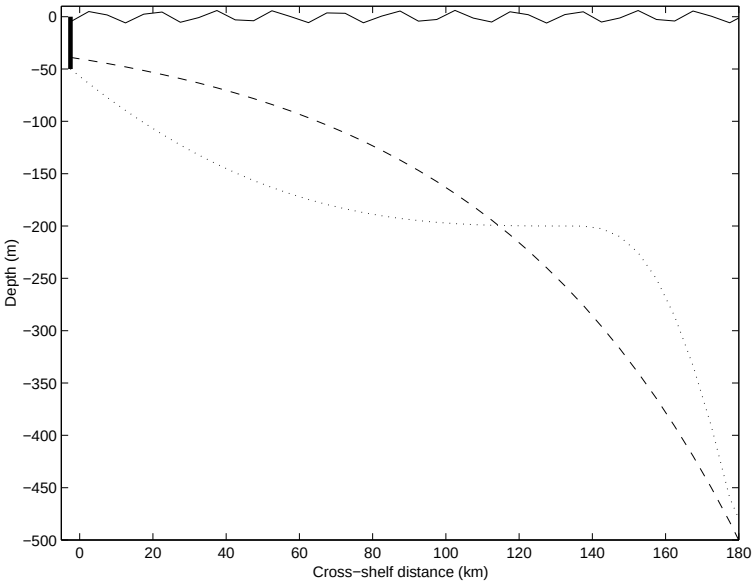

Figure 2.14 Comparison between the topography in the bay described in section (2.2)(dotted line) and the exponential topography for $H_{max} = 500$ m and $\lambda = 7 \times 10^{-6}$ (dashed line).

the detachment process is likely to be related to the presence of these standing shelf waves. Nevertheless, these wavelengths increase when the width of the shelf (Y_{max}) decreases. This is in disagreement with the pattern observed in section (2.6.3).

2.8.3 Standing shelf waves excitation

In this section, I would like to propose and illustrate a possible process for standing waves excitation in the lee of a cape. To do so, the linear vorticity equation (2.27) is supposed valid even in the close vicinity of the cape. This linear problem implies that the moving cape does not carry in its movement any water in its wake, and thus does not generate any net transport. Because the cape moves in a channel bounded by a wall offshore, mass conservation implies that, looking from the frame related to the cape, the current in front of the tip of the cape is greater than the current (U_0) associated to the motion of the cape. The velocities at the tip of the cape are supposed constant and equal to U_1. One can imagine that the flow is redistributed inside a frictional boundary layer close to the cape. For example, the lateral boundary layer thickness defined by Becker [1991], dimensionalized by the size of the cape, is here around 5 kilometers. This is one order of magnitude smaller than a characteristic wave length. If we keep the topography defined in the previous section, global mass conservation for a cape of cross-shelf extension Y_{cap} implies:

$$\int_{Y_{cap}}^{Y_{max}} HU_1 \, dy = \int_{0}^{Y_{max}} HU_0 \, dy \tag{2.41}$$

Giving U_1 as a function of U_0:

$$U_1 = U_0 \frac{1 - e^{-2\lambda Y_{max}}}{1 - e^{-2\lambda (Y_{max} - Y_{cap})}} \tag{2.42}$$

The velocity (U_1) offshore of the cape and the presence of the cape at x=0 imply that the along shore velocity, solution of the vorticity equation (2.27), must have equal values at x=0

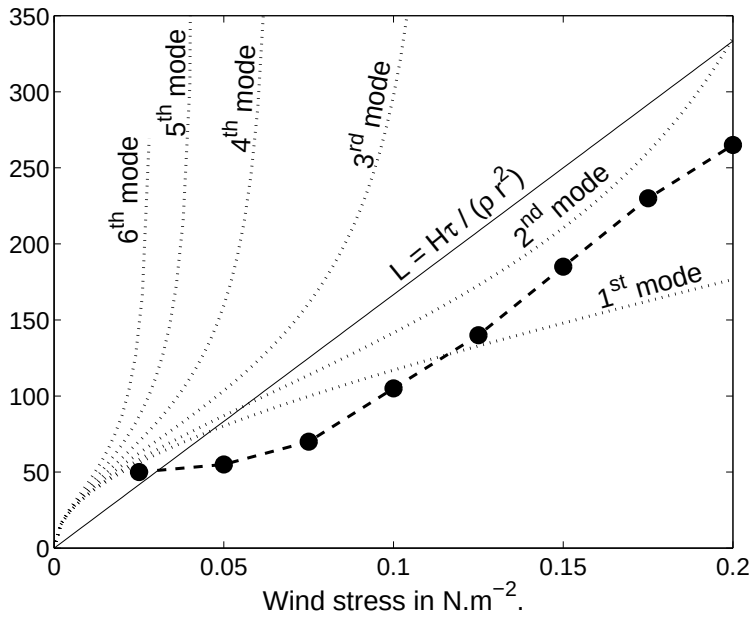

Figure 2.15 Standing wave lengths for first 6 modes as a function of wind stress for a bay of 180 km wide ($H_{max} = 500$ m and $\lambda = 7 \times 10^{-6}$). Comparison with the size of the eddy for a cape of 100 km.

(in the frame moving with the cape):

$$U_{wave} = \begin{cases} -U_0 & \text{for } 0 < y < Y_{cap} \\ U_0 \left(\frac{1-e^{-2\lambda Y_{max}}}{1-e^{-2\lambda(Y_{max}-Y_{cap})}} - 1 \right) & \text{for } Y_{cap} < y < Y_{max} \end{cases} \tag{2.43}$$

This implies a wave solution in the same order of magnitude of U_0. Hence, the term $\frac{U_0 R_0}{U} \frac{\partial \vec{u}}{\partial x}$ has the same importance as the term $R_0(\vec{u}.\nabla)\vec{u}$ in the addimentional momentum equation (2.25). Solving the linear vorticity equation (2.27), applying the boundary condition (2.43) for x=0, is equivalent asking if a set of linear propagating waves can account for the flow generated just at the back of a moving cape. The frictional boundary layer is no longer necessary to explain the redistribution of the flow behind the cape; this can be done by a set of linear standing waves. The boundary condition at x=0 for the transport stream function accounting for the lee shelf waves is:

$$\psi_w(0,y) = \begin{cases} \frac{U_0 H_{max} e^{-2\lambda Y_{max}}}{2\lambda} \left(e^{2\lambda y} - 1 \right) & \text{for } 0 < y < Y_{cap} \\ \frac{U_0 H_{max} e^{-2\lambda Y_{max}}}{2\lambda} \left(\frac{1-e^{2\lambda Y_{cap}}}{1-e^{-2\lambda(Y_{max}-Y_{cap})}} \right) \left(e^{-2\lambda(Y_{max}-y)} - 1 \right) & \text{for } Y_{cap} < y < Y_{max} \end{cases} \tag{2.44}$$

One can note that $\psi_w(0,y)$ is continuous and that $\psi_w(0,0) = \psi_w(0,L) = 0$, in agreement with the properties of the standing waves. For the following we will define $\psi_0 = \frac{U_0 H_{max} e^{-2\lambda Y_{max}}}{2\lambda}$ and $\psi_1 = \frac{U_0 H_{max} e^{-2\lambda Y_{max}}}{2\lambda} \left(\frac{1-e^{2\lambda Y_{cap}}}{1-e^{-2\lambda(Y_{max}-Y_{cap})}} \right)$.

For x=0, pressure and transport should be both continuous. In this case, although pressure can be obtained from the along shore momentum equation, there is no information for the pressure for $x \leq 0$. This information could be obtained by deriving also a wave solution upstream of the Cape (where the mean current is U_1). To stay simple, we will keep only local conservation of the transport for the matching conditions at x=0. This gives:

$$\psi_w(0,y) = \sum_{n=1}^{\infty} A_n e^{\lambda y} sin\left(\frac{n\pi y}{Y_{max}}\right) \tag{2.45}$$

Because $\frac{2}{Y_{max}} \int_0^{Y_{max}} sin\left(\frac{n\pi y}{Y_{max}}\right) sin\left(\frac{m\pi y}{Y_{max}}\right) dy = \delta_{mn}$, we obtain:

$$A_n = \frac{2}{Y_{max}} \int_0^{Y_{max}} sin\left(\frac{n\pi y}{Y_{max}}\right) e^{-\lambda y} \psi_w(0,y)\, dy \tag{2.46}$$

Introducing the value of $\psi_w(0,y)$:

$$A_n = \frac{2}{Y_{max}} \left(\psi_0 B_n - \psi_0 C_n + \psi_1 e^{-2\lambda Y_{max}} D_n - \psi_1 E_n\right) \tag{2.47}$$

With,

$$\begin{array}{rcl} B_n & = & \int_0^{Y_{cap}} e^{\lambda y} sin\left(\frac{n\pi y}{Y_{max}}\right) dy \\ C_n & = & \int_0^{Y_{cap}} e^{-\lambda y} sin\left(\frac{n\pi y}{Y_{max}}\right) dy \\ D_n & = & \int_{Y_{cap}}^{Y_{max}} e^{\lambda y} sin\left(\frac{n\pi y}{Y_{max}}\right) dy \\ E_n & = & \int_{Y_{cap}}^{Y_{max}} e^{-\lambda y} sin\left(\frac{n\pi y}{Y_{max}}\right) dy \end{array} \tag{2.48}$$

To confirm the validity of the assumptions made previously, a numerical experiment using SCRUM has been conducted. The configuration is the same as the reference experiment described in the section (2.4), except for the bottom topography and the value of the wind forcing. In this experiment, the bottom topography follows the equation (2.32) with $H_{max} =$ 500 m and $\lambda = 7 \times 10^{-6}$ (see figure 2.14). The value of the constant wind stress is fixed at 0.05 N.m^{-2}. The solution is stationary after 50 days, thus a transport stream function can be extracted from the model outputs. The transport stream function and the barotropic velocities in the lee of the cape, for the model at day 100, are shown on figure (2.17-a). Using this topography, no recirculation is visible, the current follows the lee side of the cape to fill the bay. Nevertheless, large standing waves remain in the lee of the cape. They exhibit wave lengths ranging from roughly 50 km in the bay up to 100 km for the small oscillations visible near the offshore boundary. The averaged value of the along shore velocities is 0.1 m.s^{-1}, which is 40 % less than the wind forced velocities expected if there was no coastline variations (equation 2.9). This accounts for the drag induced by the cape on the wind forced circulation. The wave pattern is rapidly damped with increasing x, and oscillations are hardly visible after 3 wave lengths. The total transport is about 3.5 Sv. The transport isocontour closest to the coast is moving slightly offshore with increasing x, due to the presence of the downstream cape associated to the periodic channel.

The mean along shore velocities of the numerical experiment (0.1 m.s^{-1}) gives the value for U_0 for the calculation of the standing wave solution. In this case, only the 5 first modes are non-evanescent. They correspond to wave lengths ranging from 61 km to 110 km (figure 2.16-a). Evanescent waves adjust the solution to the boundary condition close to the cape. Their amplitudes being small (figure 2.16-b), they do not strongly affect the solution in the bay. The computation of the relative difference between the solution at x=0 and the boundary condition (figure 2.16-c) shows that 17 modes are sufficient to have a solution close to the boundary condition at x=0. The graph (2.16-b) shows that most of the solution in the bay is picked up by the first mode. The wave length of this mode is 61 km, which is close to the value of the size of the eddy for this wind stress. The solution given by summing the 20 first shelf waves modes and the mean along shore current is represented on figure (2.17-b). The

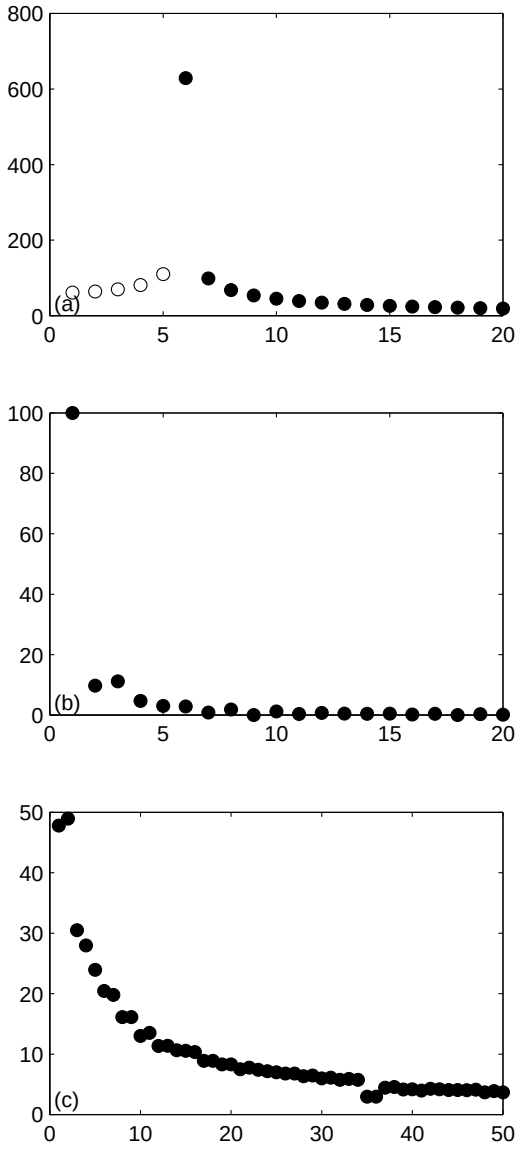

Figure 2.16 Properties of the standing waves. a: Wavelengths in kilometers for the 20 first modes; the black dots accounts for the evanescent waves (in this case, it is the e-folding length that is represented). b: Amplitude relative to the first mode in percent of the 20 first modes; note that the seventh mode amplitude is already less than 1% than the first mode amplitude. c: Total difference in percent between the boundary condition and the wave solution in x=0; there is less than 10% difference after 17 modes added.

wave pattern close to the cape and the waves length are consistent with the numerical result (figure 2.17-a), but no damping of the waves occurs in the bay. On the contrary, variations happen to increase with increasing x in the first 300 km. This difference is due to the absence of bottom friction when deriving the wave solution. The effect of bottom friction can be roughly simulated by introducing an exponential damping for each wave mode. A scaling of the effects of bottom friction versus the advection by the mean current gives an e-folding length X_0:

$$\frac{U_0^2}{X_0}\frac{\partial u'}{\partial x'} \sim -\frac{rU_0}{H_0}u' \Rightarrow X_0 = \frac{rU0}{H_0} \tag{2.49}$$

Where H_0 is the mean value of the bottom topography and r is the linear bottom friction parameter defined in section (2.2). This gives an e-folding length of 50 km. The new solution is shown on figure (2.17-c). It coincides relatively closely to the numerical solution (figure 2.17-a). This result confirms the assumptions made in deriving the standing waves equation and emphasizes the importance of bottom friction. Another discrepancy is the difference between the numerical and standing wave solutions for the incoming current at x=0. A remedy should be to resolve the standing wave dynamics upstream of the cape and to add a boundary condition on the free surface at x=0 as explained previously.

This analysis shows that a local mass conservation condition is sufficient to generate standing waves forced by a mean current in the lee of a cape. Although stratification is not taken into account, this may be an explanation of the large scale stationary features observed in the upwelling front in the lee of Cape Columbine [*Shannon,* 1985].

2.8.4 Standing edge waves ?

Whereas the presence of standing shelf waves and a balance advection/bottom friction can explain the flow pattern in the lee of capes of an order of magnitude of 100 km, this is not satisfactory in the case of small capes. For small capes, perturbations develop in the bay close to shore, where the bottom topography follows a law corresponding more to:

$$H = H_{max}\left(1 - e^{-\lambda y}\right) \tag{2.50}$$

accounting for a flat shelf rising at the coast. Ball [1967], derived the linear barotropic equations of motion over this topography for along shore propagating waves with no offshore limit. He found solutions in the form of edge waves. The same approach is applied in the case of standing waves. Therefore, as in section (2.8.2), we look for solutions in the standing wave form Ye^{ikx}, where Y is a function of y only. Introducing this form for each variable in the linear equations of motion (2.26), we obtain the system:

$$\left\{\begin{array}{rcl} ikU_0u - fv &=& -ikg\zeta \\ ikU_0v + fu &=& -g\frac{\partial \zeta}{\partial y} \\ ikHu + \frac{\partial Hv}{\partial y} &=& 0 \end{array}\right. \tag{2.51}$$

Where all the variables are now only y-dependent. The solution of the system (2.51) for ζ (the linear vorticity equation) is:

$$H\frac{\partial^2 \zeta}{\partial y^2} + \frac{\partial H}{\partial y}\frac{\partial \zeta}{\partial y} - \left(Hk^2 + \frac{\frac{\partial H}{\partial y}f}{U_0}\right)\zeta = 0 \tag{2.52}$$

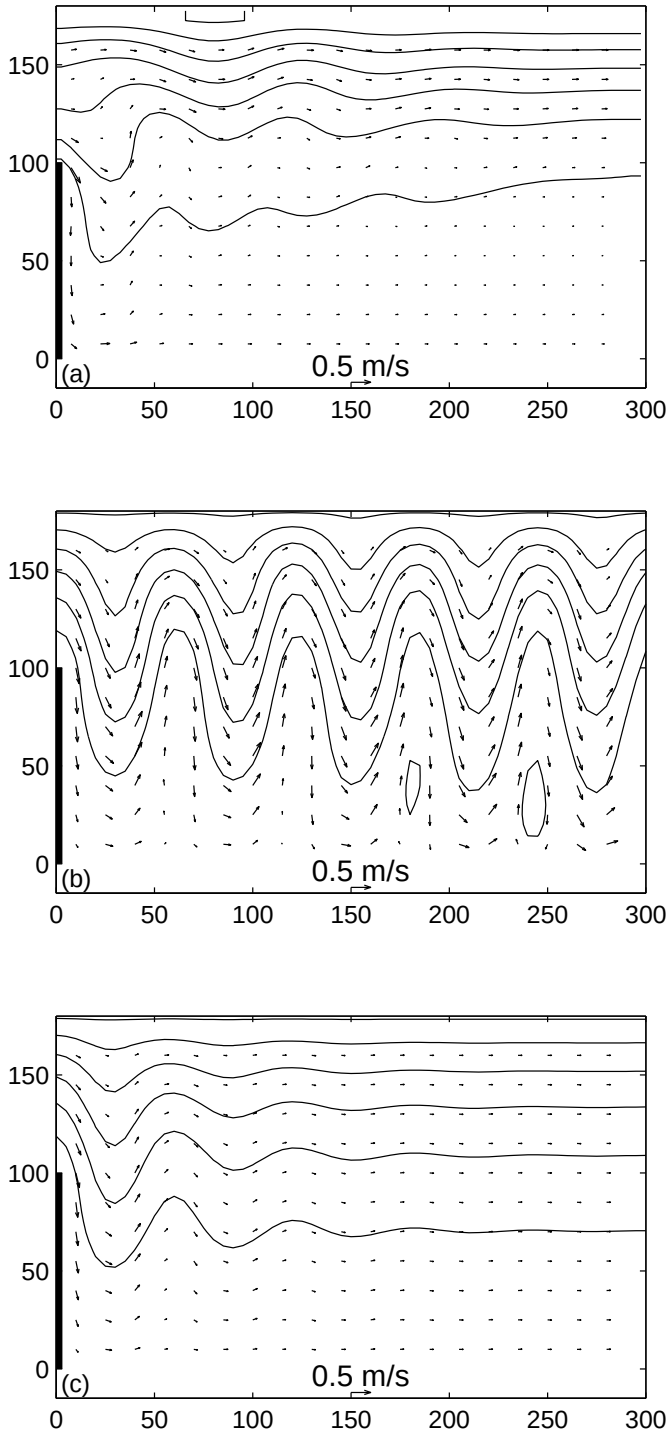

Figure 2.17 Transport stream function and barotropic velocities in the lee of a cape of 100 km width over an exponential bathymetry. a: Output at day 100 for a numerical experiment forced by an along shore wind stress of 0.05 N.m^{-2}. b: Standing waves solution for an along shore current $U_0 = 0.1$ m.s^{-1}. c: Same as b with the waves damped with an e-folding along shore length of 50 km. In each portrayal, the interval between the isolines is 0.5 Sv.

with ζ finite at the coast and zero at infinity. Introducing the value of H and applying the variable transformation:

$$s = e^{-\lambda x} \tag{2.53}$$

We obtain:

$$s^2(1-s)\frac{\partial^2\zeta}{\partial s^2} + s(1-2s)\frac{\partial\zeta}{\partial s} - \left[\frac{k^2}{\lambda^2} + \left(\frac{f}{\lambda U_0} - \frac{k^2}{\lambda^2}\right)s\right]\zeta = 0 \tag{2.54}$$

Following Ball [1967], this equation accepts solutions in the form:

$$\zeta = s^p \sum_{j=0}^{\infty} A_j s^j \tag{2.55}$$

where

$$p^2 = \frac{k^2}{\lambda^2} \tag{2.56}$$

and

$$\frac{A_{j+1}}{A_j} = \frac{(j+p+1)(j+p) + \frac{f}{\lambda U_0} - p^2}{(j+p+1)^2 - p^2} \tag{2.57}$$

In order to keep ζ finite for $y \to \infty$, we must have $p > 0$. The ratio (2.57) shows that the series (2.55) is divergent unless it terminates. To terminates the series, an integer n must exist such that:

$$(n+p+1)(n+p) + \frac{f}{\lambda U_0} - p^2 = 0 \tag{2.58}$$

Thus, selecting the wavelengths of the standing edge waves:

$$L_n = -\frac{2\pi}{\lambda}\frac{1+2n}{n(n+1) + \frac{f}{\lambda U_0}};\ n = 0, 1, 2, 3, ... \tag{2.59}$$

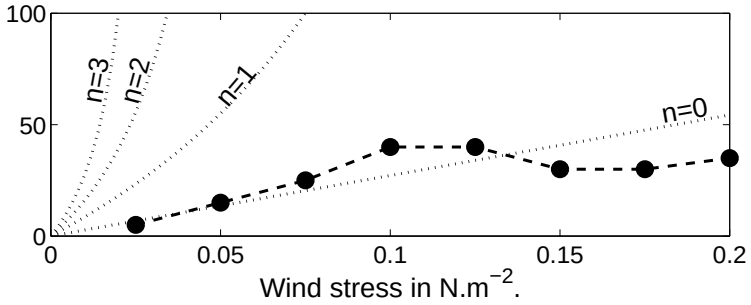

Figure 2.18 Standing edge wave lengths for the 4 first orders has a function of the wind stress. Comparison with the size of the eddy for a cape of 25 km.

λ as been chosen equal 6×10^{-5} to compare the result with the size of the perturbation for a cape of 25 km. We can note on figure (2.18) that the zero order edge wave length coincides

with the size of the eddy. This shows that smaller capes force this other kind of waves. It explains the differences for the eddy size found between the different capes in figure (2.11).

To summarize, it has been demonstrated in this last section that although flat bottom dynamics control the recirculation in the bay, topographic waves are key phenomena in the barotropic detachment process on the shelf. Because they occur only in presence of an equatorward current (at the eastern boundary of an ocean), they can induce a dissymetry in the drag if the forcing oscillates. This can produce a poleward net current in some places.

2.9 Retention induced by the attached barotropic eddy

2.9.1 The "water age" tracer

To illustrate the effects of the development of the eddy on the coastal and offshore circulation, a tracer T has been introduced in the model. It follows a time forced advective equation:

$$\frac{\partial T}{\partial t} + \bar{u}\frac{\partial T}{\partial x} + \bar{v}\frac{\partial T}{\partial y} = 1 \tag{2.60}$$

The number 1 on the right of equation (2.60) is the time forcing term. To be consistent with the numerical SCRUM model, the equation (2.60) has been rewritten in the flux form and for the sake of numerical stability, biharmonic viscosity has been included.

$$\frac{\partial}{\partial t}(DT) + \frac{\partial}{\partial x}(D\bar{u}T) + \frac{\partial}{\partial y}(D\bar{v}T) = D + \nu_4\hat{\triangle}\left(\frac{\hat{\triangle}(T)}{D}\right) \tag{2.61}$$

ν_4 has been kept as small as possible, and because in all experiments Re_{biharm} is of the order of $O(10^5)$, viscosity should not perturb the solution. T is kept at zero at the upwind boundary. Away from the boundary, T increments continuously. To test this, T has been introduced in an experiment with a rectilinear coastline and a flat bottom. Using the former analytical results, at day 50, when the solution is stationary (equation 2.9), the time since a water particle has left the upwind boundary is only x-dependent:

$$T = \frac{\rho r x}{\tau} \tag{2.62}$$

The rectilinear coastline numerical experiment is in agreement with this solution (figure not shown).

From the outputs at day 100 of the reference experiment, we can see that the distribution of T over the model domain is strongly influenced by the topography and the development of the eddy in the lee of the cape (figure 2.19-b). In the offshore area (y>200 km), T increases almost linearly towards the right side of the domain (the downwind and equatorward directions), this illustrates the advection of the water as it flows toward the equatorward side of the model domain. In the coastal area, T reaches a maximum (90 days) in the vicinity of the cape (x=40 km, y=100 km) and in the downstream near-shore area (figure 2.19-b, T=60 days, x=80 km, y=90 km). It reaches a local maximum inside the shelf break meander where the velocities are weak (figure 2.19-b, T=45 days, x=170 km, y=160 km). For a wind 50% stronger than the reference experiment, whereas the area of strong T values has increased with the size of the eddy, the maximal value of T does not vary significantly from the reference experiment (figure 2.19-c). In this experiment, the local maximum on the shelf edge has disappeared. For a wind 50% weaker, the eddy is small (<40 km) and its contribution

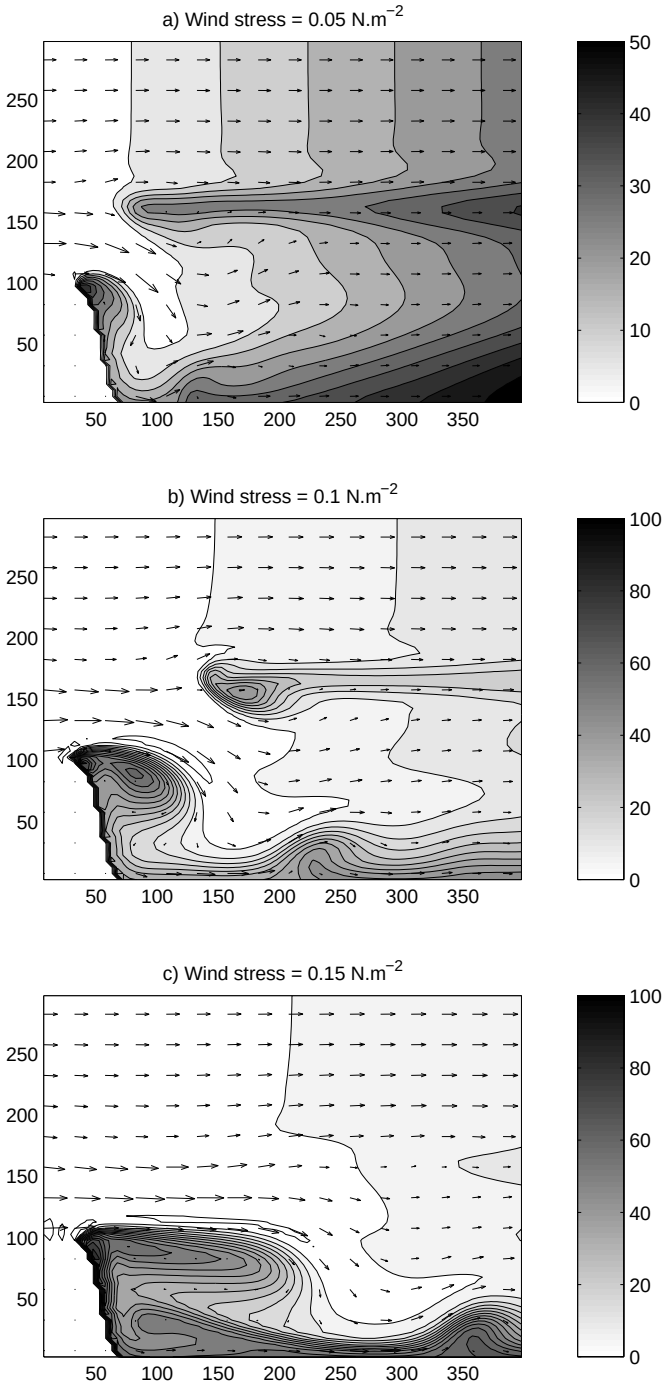

Figure 2.19 Spatial distribution of the water age tracer at day 100 for experiments similar to the reference experiment. The along shore wind stress is fixed during each experiment at: (a) 0.05 N.m^{-2}, (b) 0.1 N.m^{-2}, (c) 0.15 N.m^{-2}. The horizontal coordinates are in kilometers and the greyscale range for the water age tracer is in days.The interval between the isolines is 5 days in each portrayal.

does not affect dramatically the tracer distribution (figure 2.19-a). Even so, there is a local maximum at the tip of the cape (figure 2.19-a, T=40 days, x=45 km, y=95 km).

In order to investigate the effects of the intensity of the wind forcing on the distribution of T, several successive runs of the model are performed using values of wind stress increasing from 0.02 N.m^{-2} to 0.2 N.m^{-2} by steps of 0.02 N.m^{-2} (figure not shown). The spatial distribution of T is extracted at day 50. For low wind forcing (ranging from 0.02 to 0.06 N.m^{-2}) and weak flow detachment, there are small differences between the coast and the offshore areas; T increases almost steadily over the entire domain towards the right boundary. For moderate wind forcing (ranging from 0.06 to 0.14 N.m^{-2}), the eddy starts to develop downwind of the cape. In the offshore area, the distribution of T is not affected by the eddy. In the coastal domain, the development of the eddy induces an increase of the age of the water retained in the eddy and on the coastal side of the eddy. T reaches a maximum value of about 30 days in the near-shore domain. For strong wind forcing (greater than 0.14 N.m^{-2}), the size of the eddy growths as the wind but T does not increase in the eddy

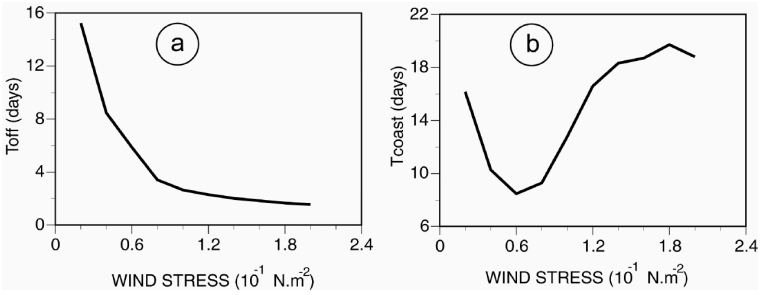

Figure 2.20 Value of the water age tracer, T_{off}(a) and T_{coast}(b) at day 50 for values of wind stress forcing ranging from 0.02 N.m^{-2} to 0.2 N.m^{-2} by steps of 0.02 N.m^{-2}.

These results are summarized on figure 2.20. In order to allow comparison between the offshore and coastal regions, T is averaged over two areas: a coastal/eddy area (T_{coast}: x=25 to 150 km and y=0 to 110 km) and an offshore area (T_{off} : x=25 to 150 km and y=110 to 200 km). T_{coast} and T_{off} are calculated at day 50 for each of the successive runs performed with wind stress ranging from 0.02 N.m^{-2} to 0.2 N.m^{-2}. In the offshore domain, T_{off} decreases as an inverse function of the wind stress: the stronger is the wind, the stronger is the advection towards the right side of the model domain [e. g. equation (2.62)]. In the coastal domain, T_{coast} decreases as the wind forcing increases from low to moderate (from 0.02 to 0.06 N.m^{-2}). In that range of wind forcing, the cape has little influence on the coastal circulation, the eddy size remains small compared to the size of the cape. For stronger wind forcing, the effect of the eddy on the coastal circulation is highly noticeable. For wind forcing ranging from 0.06 to 0.14 N.m^{-2}, the size of the eddy expands and T_{coast} increases simultaneously with the wind. From 0.14 to 0.2 N.m^{-2}, the size of the eddy reaches or expands over the domain where T_{coast} is calculated and T_{coast} reaches a plateau at a value of 18 days.

The variability of T_{coast} and T_{off} over a wide range of wind forcing illustrates the effects of the development of the eddy on the coastal and offshore circulation. When the wind forcing is strong enough (greater than 0.06 N.m^{-2}), the eddy induces a pronounced recirculation in the coastal domain, but the offshore area is unaffected. Looking back at figure 2.2, one can see that while some water may enter the eddy as a slow equatorward flow near-shore, most of the water has circulated around the eddy and then entered from the bay side. The relative increase of T in the coastal eddy domain, when compared to the value in the offshore area, is an important consequence of the development of the eddy.

2.9.2 A retention index

The presence of the eddy contributes to the formation of two distinct patterns of circulation within the model domain: in the offshore area, the circulation is predominantly along shore; in the coastal area, the circulation is dominated by a cyclonic eddy and by the associated recirculation pattern. The size of the eddy is positively related to the intensity of wind forcing. The recirculation induced by the eddy tends to isolate the near-shore area from the offshore domain. It limits the cross-shelf exchange of water and retains water particles within the coastal domain, thus providing a mechanism for retention. Retention in this coastal domain is then closely related to the wind induced recirculation pattern. The next step in our analysis is to evaluate the strength of retention as a function of the strength of the wind forcing.

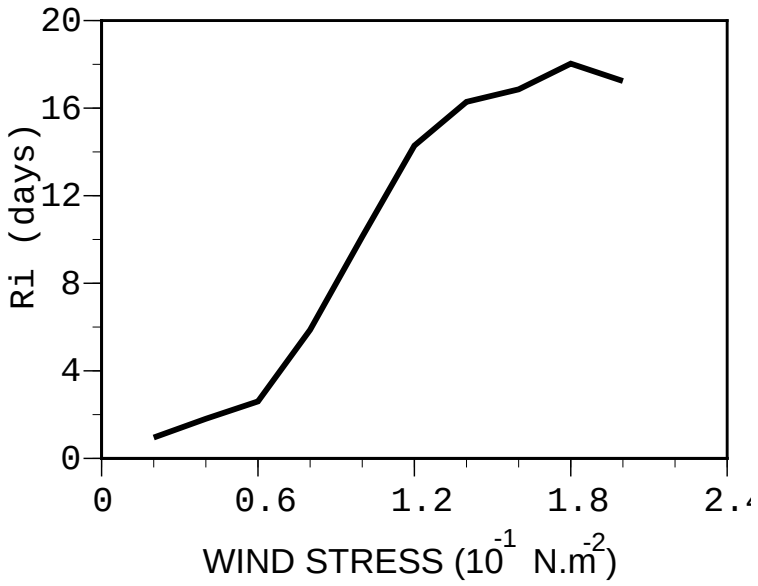

Figure 2.21 The relationship between the retention index R_i and wind stress, ranging from 0.02 N.m^{-2} to 0.2 N.m^{-2} by steps of 0.02 N.m^{-2}.

A true retention index would have been given by the residence time computed from the advection fields provided by the model. However, the difference between the age of the water in the coastal domain (T_{coast}) and the offshore domain (T_{off}) can be used as a proxy to evaluate the intensity of the retention. The variability of this index (further noted as R_i) gives an indication on how the aging of the water differs between the two areas, a positive (negative) value indicates water particles being older (younger) in the coastal domain relative to the offshore area. From a biological point of view, this offshore-inshore gradient can be used to evaluate the potential advantage for larvae to be located in the coastal area. The variability of R_i as a function of wind stress is presented on figure 2.21. R_i increases as the wind forcing increases, it reaches a maximum (18 days) value for a wind stress of 1.8 N.m^{-2} and then appears to level off or decrease. As mentioned before, R_i represents the difference between the coastal and the offshore areas in the aging process of the water particles and R_i should not be used as an indicator of residence times within the bight.

This positive relationship between wind forcing and the retention index suggests that, in an upwelling system, circulation patterns such as a standing vortex may provide retention in the lee side of a cape. Further, stronger upwelling favorable winds can enhance retention within the near-shore area despite the intensification of the offshore flow related to the up-

welling. Such structures, providing a positive coupling between upwelling and retention, have been documented in several upwelling systems [*Graham and Largier,* 1997, *Roy,* 1998].

In the Benguela upwelling system, most of the spawning occurs in late spring and summer, during the peak season of the upwelling. Fish eggs and larvae are transported from the spawning ground to the West Coast upwelling by a coastal jet. With the classical wind-driven coastal upwelling circulation structure of offshore transport of surface water, larvae will tend to be transported in the offshore domain and be lost. However, our modeling experiment shows that the Cape Columbine plume and the associated coastal recirculation in St Helena Bay provide a retention mechanism allowing the larvae to be retained within the productive coastal domain and thereby to avoid dispersion in the offshore area.

2.10 Summary

We used an idealized numerical model to understand the interactions between the wind-induced circulation on the shelf and topographical features such as Cape Columbine and St. Helena Bay. The setting of the model is based on the assumption that the circulation on the shelf follows barotropic dynamics. Hence, the barotropic equations of motion have been solved in a periodic channel and over an analytical bathymetry. They have been constrained by a constant upwelling favorable wind stress and a linear bottom friction. Despite these simplifications, it appears that the model is able to produce a cyclonic eddy in St. Helena Bay that corresponds to the observed circulation pattern [*Holden,* 1985, *Shannon,* 1985, *Boyd and Oberholster,* 1994]. The shape and size of this eddy are in relative agreement with the results of Oey [1996] and Boyer and Tao [1987a]. The eddy creates a dynamical barrier, limiting the exchanges between the near-shore area and the shelf edge domain.

Diagnostic analysis shows that the recirculation process is controlled by a balance between the Coriolis acceleration and the pressure gradient. The velocities offshore are linked to a balance between wind stress and bottom friction and the external part of the eddy follows cyclo-geostrophic dynamics. When the numerical solution reaches a stationary state, a vorticity analysis reveals that a balance between the curl of advection and the curl of bottom friction controls the eddy dynamics. This balance gives a characteristic eddy length scale proportional to the wind stress and inversely proportional to the square of the linear bottom friction parameter. Several numerical experiments using a wide range of wind stress and bottom friction values, indicate that the along shore extension of the eddy follows the trends of this length scale when the dynamics are in the attached-cyclonic-eddy regime. The influence of the size of the cape has been tested, showing different regimes of perturbations. Different kinds of standing coastal trapped waves, in equilibrium with a mean along shore current have been proposed to explain the resulting flow patterns in the bay. An analytical solution has been derived to explain the standing shelf wave excitation by a mean along shore current past a cape. A barotropic tracer representing the sea surface temperature has been introduced into the model to illustrate the impact of an attached barotropic cyclonic eddy on the generation of upwelling plumes

A tracer showing the age of the water is introduced to evaluate the intensity of recirculation generated by the eddy in the coastal domain. This tracer is used as a proxy for retention and to explore the relation between the intensity of retention and wind forcing. In accordance with previous observations, the model simulation indicates that the topography induces retention in the lee side of the cape. In regions where fish spawning occurs during the upwelling season, fish have successfully used such structures to reproduce [*Roy et al.,* 1989, *Bakun,* 1996, *Bakun,* 1998]. In the Benguela upwelling system, St Helena

Bay is recognized as the main nursery ground off the West coast where juvenile fish are concentrated [*Hutchings,* 1992], suggesting that this retention mechanism may be critical to recruitment success.

This idealized work provides a conceptualized portrayal of some typical processes that we can encounter in St. Helena Bay.